

Faculty of Physics and Astronomy
Ruprecht-Karls-University Heidelberg

Bachelor Thesis
in Physics

submitted by
Fabian Krämer
born in Heidelberg

December 2023

Development and characterization of an integrated two-stage dc-SQUID for the read-out of metallic magnetic calorimeters

This Bachelor thesis was carried out by Fabian Krämer
at the Kirchhoff-Institute for Physics
under the supervision of
Prof. Dr. C. Enss

This thesis discusses the development and characterization of an integrated two-stage dc-SQUID setup, optimized for the readout of metallic magnetic calorimeters. For this purpose, a current sensor dc-SQUID designed in the research group with an input inductance of $L_i = 6 \text{ nH}$ and an adapted 18-cell dc-SQUID series array were utilized. The current sensor SQUID is implemented as a second-order parallel gradiometer and can be connected to a magnetic calorimeter via a superconducting flux transformer. The 18-cell SQUID series array consists of first-order gradiometers that are connected in a serial circuit and was employed as an amplifier in the two-stage SQUID setup. The integrated two-stage dc-SQUID setup was characterized at temperatures of $T = 4.2 \text{ K}$ and $T = 10 \text{ mK}$. For the integrated two-stage dc-SQUID setup, a flux-to-voltage transfer coefficient of $V_\Phi = 2170 \mu\text{V}/\Phi_0$ and a flux-to-flux transfer coefficient of $G_\Phi = 1.94$ were measured at 4.2 K. Additionally a white noise of $\sqrt{S_{\Phi,w}} = 0.482 \mu\Phi_0/\sqrt{\text{Hz}}$ and a $1/f$ noise of $\sqrt{S_{\Phi,1/f}(1\text{Hz})} = 2.2 \mu\Phi_0/\sqrt{\text{Hz}}$ with an exponent $\alpha = 0.8$ for the low-frequency noise component were determined at 10 mK. The performance of the integrated two-stage SQUID is thereby comparable to two-stage designs on distinct chips previously produced within the research group and is already being utilized in the AMoRE experiment.

Entwicklung und Charakterisierung eines integrierten zweistufigen dc-SQUIDs zur Auslese metallisch magnetischer Kalorimeter

In der vorliegenden Arbeit wird die Entwicklung und Charakterisierung eines integrierten zweistufigen dc-SQUID Aufbaus, optimiert für die Auslese von metallischen magnetischen Kalorimetern, beschrieben. Dafür wurde ein in der Arbeitsgruppe entworfenes Stromsensor-dc-SQUID mit einer Eingangsinduktivität von $L_i = 6 \text{ nH}$ und ein angepasstes 18-Zellen dc-SQUID Serien-Array verwendet. Das Stromsensor-SQUID ist als Parallelgradiometer zweiter Ordnung ausgeführt und kann über einen supraleitenden Flusstransformator an ein magnetisches Kalorimeter gekoppelt werden. Das 18-Zellen SQUID Serien-Array besteht aus einer Reihenschaltung von Gradiometern erster Ordnung und wurde als Verstärker in dem zweistufigen SQUID-Aufbau eingesetzt. Der integrierte zweistufige dc-SQUID Aufbau wurde bei Temperaturen von $T = 4.2 \text{ K}$ und $T = 10 \text{ mK}$ charakterisiert. Für den integrierten zweistufigen dc-SQUID Aufbau wurde dabei ein Fluss-zu-Spannungs Transferkoeffizient von $V_\Phi = 2170 \mu\text{V}/\Phi_0$ und Fluss-zu-Fluss Transferkoeffizient von $G_\Phi = 1.94$ bei 4.2 K, sowie ein weißes Rauschen von $\sqrt{S_{\Phi,w}} = 0.482 \mu\Phi_0/\sqrt{\text{Hz}}$ und ein $1/f$ Rauschen von $\sqrt{S_{\Phi,1/f}(1\text{Hz})} = 2.2 \mu\Phi_0/\sqrt{\text{Hz}}$ mit einem Exponenten $\alpha = 0.8$ für den niederfrequenten Rauschanteil bei 10 mK gemessen. Die Performanz des integrierten zweistufigen SQUIDs ist damit mit zuvor in der Arbeitsgruppe hergestellten zweistufigen Designs auf separaten Chips vergleichbar und findet bereits Anwendung im AMoRE Experiment.

Contents

1	Introduction	1
2	Theoretical Background	3
2.1	Superconductivity and Flux Quantization	3
2.2	Josephson Junction	5
2.2.1	Josephson Equations	5
2.2.2	Current-Voltage Characteristic	7
2.2.3	Short Josephson Junction in a Magnetic Field	8
2.2.4	Resistively and Capacitively Shunted Junction-Model	10
2.3	Superconducting Quantum Interference Devices	13
2.3.1	Zero Voltage State	14
2.3.2	Voltage State	16
2.3.3	Characteristic Parameters	16
2.3.4	SQUID Noise	18
3	Experimental Methods	21
3.1	Operation of dc-SQUIDS	21
3.1.1	Linearization of the dc-SQUID Signal	21
3.1.2	Two-Stage Setup	23
3.2	Experimental Setup	25
3.3	Characterization	27

4 Design of the Two-Stage SQUID	29
4.1 First-Stage SQUID	29
4.2 18-cell dc-SQUID Array	32
4.3 Integrated Two-Stage Design	33
5 Experimental Results	37
5.1 Characterization of the 18-Cell dc-SQUID Array	37
5.1.1 I/V -Characteristics of the SQUID Array	37
5.1.2 Φ/V -Characteristics of the SQUID Array	39
5.2 Characterization of the First-Stage SQUID in the Two-Stage Setup	40
5.2.1 I/V -Characteristics of the First-Stage SQUID	40
5.2.2 $\Phi_{\text{SQ}}/I_{\text{SQ}}$ -Characteristics of the First-Stage SQUID	42
5.3 Integrated Two-Stage Setup	44
5.4 Noise	46
5.4.1 Noise of the SQUID Array	46
5.4.2 Noise of the Integrated Two-Stage Setup	47
6 Summary and Outlook	51
Bibliography	53

1. Introduction

Superconducting Quantum Interference Devices (SQUIDs) are currently the most precise tools for measuring magnetic flux changes while also providing a broad bandwidth. Consequently, SQUIDs are the preferred method for highly sensitive determination of all physical quantities that can be easily converted into magnetic flux at low temperatures. Applications for these include for example medical imaging [Ste06], geophysics for subsurface exploration [Sto21] and material characterization [Rus12]. Additionally, they are of significant importance as sensitive and broadband current sensors in the operation of low-temperature particle detectors [Ens05a]. Particularly noteworthy in this context are metallic magnetic calorimeters (MMCs) [Fle05], which exhibit excellent energy resolution across a wide energy bandwidth. Such calorimeters contain an absorber, whose temperature increases after the absorption of a particle and the resulting temperature change is detected by a paramagnetic temperature sensor situated in a weak magnetic field. This temperature change is translated into a change in the magnetization of the sensor. For readout, the detector signal is magnetically coupled into a current sensor SQUID through a superconducting flux transformer. One prominent example is the AMoRE¹ experiment [Bha12], which utilizes MMCs with SQUIDs as readout sensors, to search for the neutrinoless double beta decay in the molybdenum isotope ^{100}Mo .

In principle, an MMC can be read out with a single SQUID, however in this case the setup would be limited in energy resolution due to noise, primarily caused by the SQUID electronics. For highly sensitive measurements like those in AMoRE and others, an improved energy resolution in readout sensors is necessary. To achieve this, two-stage setups can be employed, which consist of one SQUID for reading the detector signal and a second SQUID as a low-noise cryogenic amplifier. A two-stage setup can be implemented either separately on two chips or integrated on a single chip. The setup on two distinct chips offers the advantage that both, the SQUID for reading the MMCs and the MMCs themselves are easier to thermalize, as the amplifier SQUID can be mounted at a considerable distance. The integrated setup, on the other hand, provides shorter signal propagation times, resulting in a larger bandwidth, and a more compact geometry. The AMoRE experiment currently uses such integrated two-stage SQUIDs for the detector readout.

Within the framework of this thesis, a two-stage setup that is compatible with the current AMoRE layout, was designed and characterized.

¹Advanced Molybdenum-based Rare process Experiment

In chapter 2, we discuss the theoretical foundations which are essential to understand the operation of a dc-SQUID. These include the quantization of magnetic flux in closed superconducting loops and the Josephson effect. This is followed by a discussion of the properties of Josephson junctions as essential components of SQUIDs, and the RCSJ model for their description. Subsequently, the characteristics of dc-SQUIDs, which are used in this work, as well as different noise contributions, are discussed.

In chapter 3, the operation of dc-SQUIDs is discussed, including a feedback technique for linearizing the output signal, as well as the two-stage dc-SQUID setup to suppress noise induced by a room-temperature amplifier. Furthermore, methods used in this work for characterizing the developed integrated two-stage setup are introduced.

The design of the two-stage setup developed in this work is described in chapter 4. Additionally, the first-stage SQUID and the amplifier SQUID used for the integrated two-stage setup are discussed. The first-stage SQUID utilized for detector readout is based on the work of [Bau22] and adapted to an input inductance of 6 nH within the work of [Kah24]. The amplifier SQUID, serving as a low-temperature amplifier for the first-stage SQUID, is an expanded 18-cell dc-SQUID array adapted within the scope of this work.

Chapter 5 presents the experimental results of the characterization of the two-stage setup designed in the course of this work. Initially, the properties of the dc-SQUID array, of the first-stage SQUID and of the two-stage setup are examined at a temperature of 4.2 K , and their characteristic curves are presented. Finally, the noise of the two-stage setup and its individual components is discussed for a temperature of 10 mK .

2. Theoretical Background

This chapter describes the theoretical background necessary to understand the basic working principles of Superconducting Quantum Interference Devices (SQUIDs), which the integrated two-stage SQUID, developed in the framework of this thesis and discussed in detail in chapter 4, is based on. At the beginning we introduce basic properties of superconductors, followed by a discussion of Josephson junctions in the form of superconductor-isolator-superconductor contacts (SIS-contact), from which the SQUIDs used in this work are constructed. Building upon this, we will discuss the operation and characteristics of a direct current- or dc-SQUID and its readout.

2.1 Superconductivity and Flux Quantization

Below a critical temperature T_c , certain materials undergo a transition into a superconducting state, in which their electrical resistance drops to zero and magnetic fields are expelled. These phenomena are described by the BCS theory [Bar57], which introduces the Cooper pair as a boson, composed of two electrons which are bound to each other due to an attractive interaction, as the carriers of the supercurrent of a superconductor. This interaction gives rise to a gap in the continuous energy spectrum such that excitations can only occur above a certain minimum energy threshold. Due to this phenomenon, current flows through superconductors without energy loss until the minimum energy required to break up the Cooper pairs is reached. According to the BCS theory, the state of Cooper pairs in a superconductor can be described by a single macroscopic wave function [Gin09]

$$\Psi(\mathbf{r}, t) = \Psi_0(\mathbf{r}, t)e^{i\phi(\mathbf{r}, t)} = \sqrt{n_s(\mathbf{r}, t)}e^{i\phi(\mathbf{r}, t)}. \quad (2.1)$$

Here $\phi(\mathbf{r}, t)$ is the phase of the wave function and $n_s(\mathbf{r}, t)$ the local density of Cooper pairs, both of which depend on position \mathbf{r} and time t . Within the framework of the BCS theory, it can be demonstrated that the magnetic flux in a superconducting ring is quantized [Lon50]. To derive the quantization of flux, we consider a superconducting ring as shown in Figure 2.1, penetrated by a magnetic field with magnetic flux density \mathbf{B} parallel to the symmetry axis of the ring. By substituting the wave function $\Psi(\mathbf{r}, t)$ from equation (2.1) into the quantum mechanical expression for electric current in a magnetic field

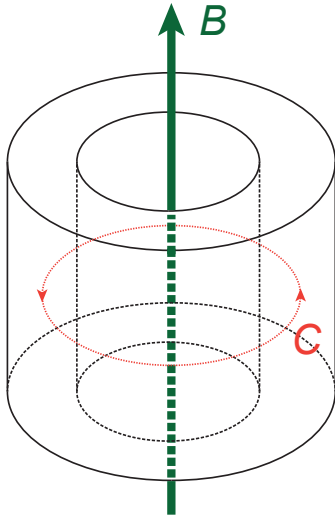


Figure 2.1: Schematic drawing of a superconducting ring, penetrated by a magnetic field with magnetic flux density \mathbf{B} parallel to the symmetry axis of the ring. The dashed red line indicates the chosen integration path C .

$$\mathbf{j} = i \frac{\hbar q}{2M} (\Psi^* \nabla \Psi - \Psi \nabla \Psi^*) - \frac{q^2}{M} \mathbf{A} \Psi^* \Psi, \quad (2.2)$$

it can be derived that the current density \mathbf{j} of the Cooper pairs in a superconductor is governed by the London equation

$$\mathbf{j} = \frac{1}{\mu_0 \lambda_L^2} \left(\frac{\hbar}{q} \nabla \phi - 2\mathbf{A} \right). \quad (2.3)$$

Here, \hbar denotes the reduced Planck constant, $q = -2e$ and $M = 2m_e$ the charge and mass of the Cooper pair, which is twice the electron charge $-e$ and mass m_e , as well as \mathbf{A} the magnetic vector potential, $\mu_0 = 4\pi \times 10^{-7} \text{ N/A}^2$ the vacuum permeability constant and $\lambda = \sqrt{M/\mu_0 n_s q^2}$ the London penetration depth. The latter of which describes the characteristic length over which the magnetic field and current density in a superconductor decay exponentially [Ens05b]. Integrating along the closed path C , as illustrated in Figure 2.1, and using Stokes' theorem we get

$$\frac{\mu_0 \lambda_L^2}{2} \oint_C \mathbf{j} d\mathbf{l} + \int_S \mathbf{B} ds = \frac{\hbar}{2e} \oint_C \nabla \phi d\mathbf{l}, \quad (2.4)$$

for which the first term on the left side of the equation vanishes if we choose the integration path deep inside the superconductor, since there the supercurrent density \mathbf{j} vanishes. The second integral on the left-hand side of equation (2.4) corresponds to the magnetic flux $\Phi = \int \mathbf{B} ds$ which passes through the loop, and the integral on the right side represents the phase difference along the integration path C . This phase difference can only take values of $2\pi n$ with $n \in \mathbb{Z}$ due to the uniquely defined nature of the wave function, which leads us to the result that the magnetic flux $\Phi = n \frac{\hbar}{2e}$

within a superconducting ring can only take integer multiples of the magnetic flux quantum $\Phi_0 = h/(2e) = 2.067\dots \times 10^{-15} \text{ Nm/A}^2$.

2.2 Josephson Junction

A Josephson junction, as schematically depicted in figure 2.2, consists of two superconducting electrodes which are characterized by weak coupling through an isolating barrier between them. This can be achieved by separating two superconducting electrodes with a few nanometers thick metal oxide layer, as done in this work using Nb/Al-AlO_x/Nb junctions.

2.2.1 Josephson Equations

The Josephson effect [Jos62a] describes the coherent tunneling of Cooper pairs through a Josephson junction, which is a potential barrier between two superconducting electrodes. If the insulating barrier is sufficiently thin, the macroscopic wave functions from equation (2.1), Ψ_1 in the electrode S₁ and Ψ_2 in the electrode S₂, as depicted in figure 2.2, overlap and couple weakly[Fey64], so that the Cooper pairs can tunnel through the barrier with no resistance. This current of Cooper pairs is the so called super current I_s in the Josephson junction. The coupling of the macroscopic wave functions Ψ_1 and Ψ_2 can be described by the two Schrödinger equations

$$i\hbar\dot{\Psi}_1 = \mu_1\Psi_1 + \kappa\Psi_2 \quad (2.5)$$

$$i\hbar\dot{\Psi}_2 = \mu_2\Psi_2 + \kappa\Psi_1, \quad (2.6)$$

where μ_1 and μ_2 describe the chemical potential of the electrodes S₁ and S₂ and κ the coupling constant which depends on material and geometry of the insulating barrier as well as the temperature. Inserting Ψ from equation (2.1) in equation (2.5) and (2.6) and separating real and imaginary part, we get the following two equations

$$\dot{n}_{s,1} = \frac{2\kappa}{\hbar}n_s \sin(\phi_2 - \phi_1) = -\dot{n}_{s,2} \quad (2.7)$$

$$\hbar(\dot{\phi}_2 - \dot{\phi}_1) = -(\mu_2 - \mu_1), \quad (2.8)$$

where $\dot{n}_{s,1} = -\dot{n}_{s,2}$ due to current conservation, and additionally we assumed that the two electrodes are identical, so the Cooper pair density n_s is the same in both electrodes and we can denote $n_1 = n_2 = n_s$. We will now use this result to derive the well known form of the two Josephson equations. Defining $\dot{n}_{s,1,2}$ as I_s , since the change in the number of Cooper pairs over time in each superconducting electrode is proportional to the supercurrent flowing through the Josephson junction, results in the first Josephson equation [Jos64], describing the supercurrent

$$I_s = I_c \sin(\varphi). \quad (2.9)$$

Here $I_c = 2\kappa n_s / \hbar$ is the critical current, up to which all current through the insulating barrier is carried by Cooper pairs and φ the gauge invariant phase difference

$$\varphi(\mathbf{r}, t) = \phi_2(\mathbf{r}, t) - \phi_1(\mathbf{r}, t) - \frac{2\pi}{\Phi_0} \int_1^2 \mathbf{A}(\mathbf{r}, t) d\mathbf{l} \quad (2.10)$$

in presence of an external magnetic or electric field [Buc04], where ϕ_1 and ϕ_2 are the phases of the macroscopic wave functions Ψ_1 and Ψ_2 , and \mathbf{A} the magnetic vector potential integrated along the path of the current as depicted in figure 2.2.

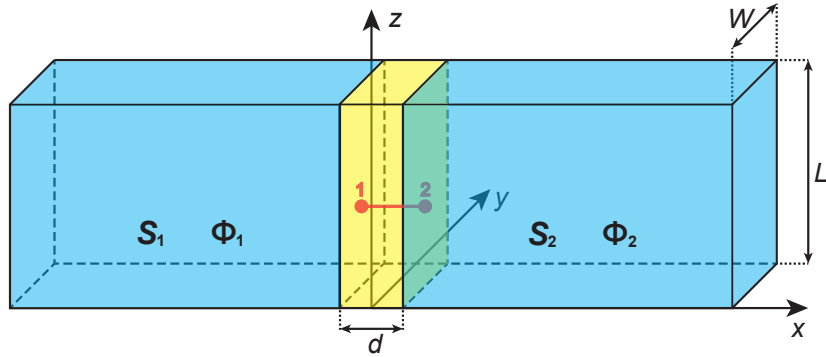


Figure 2.2: Sketch of a superconductor-insulator-superconductor (SIS) Josephson junction. S_1 and S_2 denote the superconducting electrodes with the corresponding phases Φ_1 and Φ_2 of the macroscopic wave functions and the red line indicates the integration path inside of the insulating barrier. The length of the sides of the contact area between the superconductor and the insulator are indicated by W and L , and d denotes the thickness of the insulating layer.

Resulting from equation (2.8), the second Josephson equation

$$\dot{\varphi} = \frac{2\pi}{\Phi_0} U \quad (2.11)$$

shows, that the change over time in the phase difference φ is connected to a voltage drop U over the Josephson junction. This results from both, the difference of the chemical potentials

$$\mu_2 - \mu_1 = 2e \int_1^2 \mathbf{E}(\mathbf{r}, t) d\mathbf{l} = 2eU, \quad (2.12)$$

where $\mathbf{E}(\mathbf{r}, t)$ is the electric field along the x -direction, and the electromagnetic induction of a time-varying field [Jos62b, And63]. Integrating equation (2.11) we see, that the phase difference from equation (2.9) and (2.11) it can be inferred that if there is no voltage drop over the Josephson junction, which is called the zero-voltage state, the dc-Josephson effect occurs, which means that φ and consequently also the supercurrent I_s are constant in time. However, integrating equation (2.11) we can see, that in the case of a constant voltage drop U , across the Josephson junction, which is called voltage-state, the ac-Josephson effect occurs where the phase difference φ grows linearly in time, such that the phase difference φ increases linearly in time, and consequently, the supercurrent I_s oscillates at the Josephson frequency

$$\nu_J = \frac{\omega_J}{2\pi} = \frac{U}{\Phi_0} \approx 483.6 \frac{\text{MHz}}{\mu\text{V}} U, \quad (2.13)$$

but can not be seen in the current-voltage characteristic of this work, due to the high frequency at even low voltages.

2.2.2 Current-Voltage Characteristic

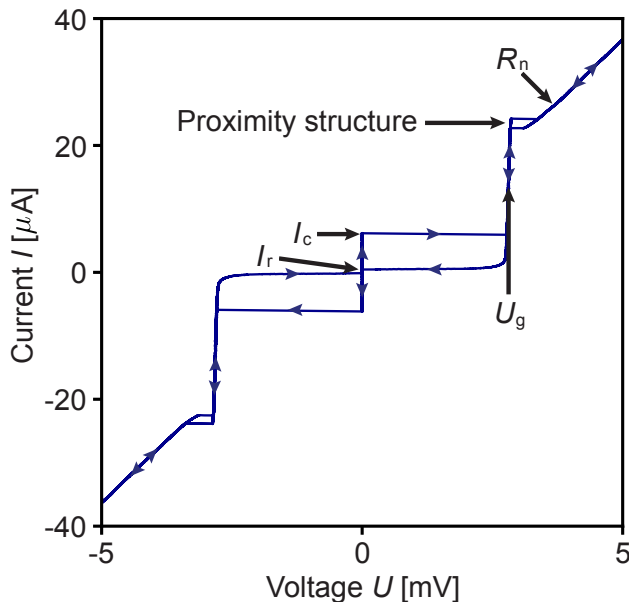


Figure 2.3: Current-voltage characteristics of a hysteretic Nb/Al-AlO_x/Nb Josephson junction measured at T=4.2K. The arrows along the curve indicate the direction in which the characteristic curve is traversed when an external current I is applied. Figure adapted from the work of [Bau22] with modifications made for the context of this thesis.

In Figure 2.3, the typical current-voltage characteristic of a Nb/Al-AlO_x/Nb junction, which was manufactured and measured in the research group [Bau22] is displayed. Starting with a current $I = 0$ applied to the junction, which is steadily increased, a supercurrent flows without resistance and voltage drop due to the dc-Josephson effect. Above the critical current $I > I_c$, there is enough energy in the

system to break up Cooper pairs which results in an additional quasiparticle current flow, associated with a voltage drop over the junction, which is evident in the current-voltage characteristic by a sharp increase in voltage at $I = I_c$ [Buc04]. In this case, the voltage across the junction is $U_g = (\Delta_1 + \Delta_2)/e$, the gap voltage, because to break up a Cooper pair, an energy of $(\Delta_1 + \Delta_2)$, which is the sum of the energy gaps of the two superconductors, must be applied. At U_g is a sharp increase in the current because when we consider the electronic density of states $D(E)$ of quasiparticles, the high density of occupied states in superconductor S1 encounters the equally high density of unoccupied states in superconductor S2. For $U \gg U_g$, the characteristic is linear because in this regime, the density of occupied and unoccupied states in both superconductors are nearly constant. In this region, the junction can be characterized by the ohmic resistance R_n with the corresponding normal current

$$I_n = \frac{V}{R_n} \quad (2.14)$$

which is carried by the quasi particles. It is important to mention that here we are considering only the linear regime for the normal current I_n , but a complete description would also include the nonlinear regime. The hysteresis structure between the gap voltage and the ohmic region is known as the proximity effect [Kla04], which results from the mutual influence of the superconducting electrodes and the normal conducting aluminum layer at their interfaces. When the current is reduced from the ohmic region, a hysteretic behavior is observed where the voltage-free state is only reached at a return current $I_r < I_c$. This is because, in addition to the Cooper pairs, thermally excited quasiparticles exist above the energy gap, which can continue to tunnel through the barrier even for $U < U_g$, until the return current is reached.

2.2.3 Short Josephson Junction in a Magnetic Field

According to equation (2.10) the gauge invariant phase difference Φ depends on the magnetic vector potential \mathbf{A} along the tunnel barrier and consequently the super current I_s from equation (2.9) can be modulated by an external magnetic field \mathbf{B} . For the short Josephson junctions used in this work, which are classified by the Josephson penetration depth [Wei69]

$$\lambda_J = \sqrt{\frac{\Phi_0}{2\pi\mu_0 j_c t_B}} \quad (2.15)$$

where $\mathbf{j}_c = I_c/A$ is the critical current density and $t_B = d + \lambda_{L,1} + \lambda_{L,2}$ the magnetic thickness of the junction with the London penetration depths of the superconductors $\lambda_{L,1/2}$, the generated magnetic self-field of the supercurrent I_s is negligible compared

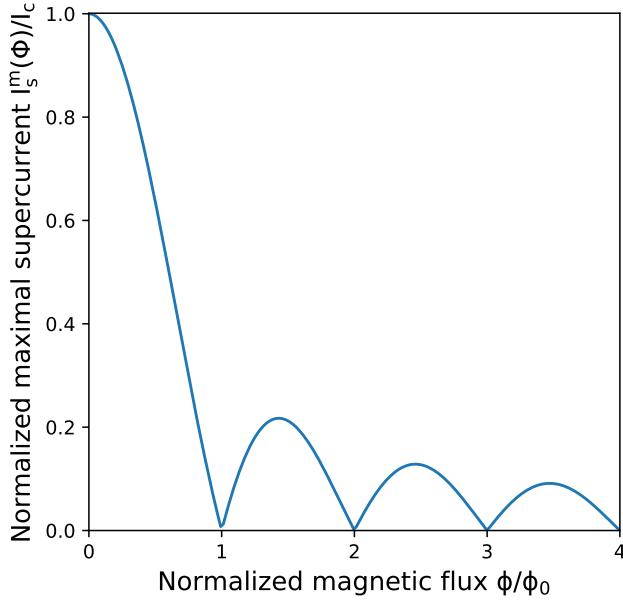


Figure 2.4: Normalized maximum supercurrent $I_s^{\max}(\Phi) / I_c$ through a rectangular Josephson junction as a function of the normalized magnetic flux Φ/Φ_0 with positive integer values and spatially constant distribution of the critical current density j_c .

to the external applied magnetic field \mathbf{B} . Here $A = WL$ is the superconductor-insulator contact area and d the isolation layer thickness as seen in figure 2.2. For a Josephson junction to be considered short, the Josephson penetration depth must be large compared to the side lengths W and L of the superconductor-insulator contact area A . Now placing A in the xy -plane and applying a magnetic field $\mathbf{B} = (0, B_y, 0)$ orthogonal to the supercurrent which goes in the x -direction and taking a closed path integral over the gradient of the phase of the superconductor wavefunction, we find according to [Jos65] the supercurrent density

$$\mathbf{j}_s(y, z) = \mathbf{j}_c(y, z) \sin\left(\frac{2\pi}{\Phi_0} t_B B_y z + \varphi_0\right) \quad (2.16)$$

where φ_0 is the phase difference at $z = 0$. Integrating the supercurrent density \mathbf{j}_s while assuming a spatially constant critical supercurrent density \mathbf{j}_c we find the equation for the maximal supercurrent

$$I_s^{\max}(\Phi) = I_c \left| \frac{\sin \frac{\pi \Phi}{\Phi_0}}{\frac{\pi \Phi}{\Phi_0}} \right| \quad (2.17)$$

which depends on the magnetic flux Φ through the junction and is plotted in figure 2.4.

2.2.4 Resistively and Capacitively Shunted Junction-Model

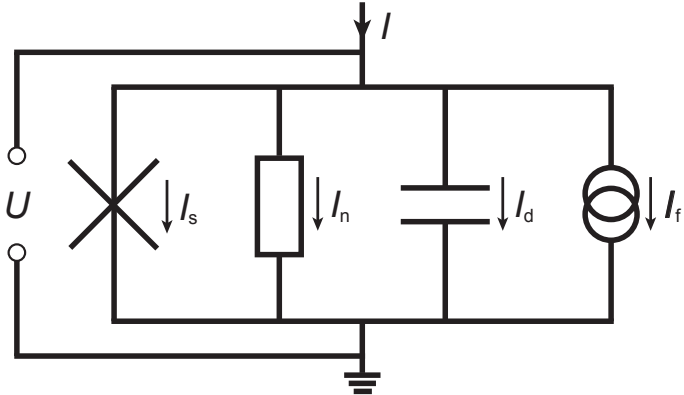


Figure 2.5: Equivalent circuit for a Josephson junction in the RCSJ model. In this model, the total current I through the junction is divided into four channels: the superconducting current I_s , the normal current I_n , the displacement current I_d , and the fluctuation current I_f . The voltage drop across the junction is denoted by U .

To model a real Josephson junction, we need to consider additional effects beyond the super current I_s and normal current I_n discussed in chapters 2.2.1 and 2.2.2, such as the capacitance of the junction and fluctuation currents. To incorporate the mentioned effects, we consider the Resistively and Capacitively Shunted Junction (RCSJ) model [McC68], as seen in the equivalent circuit diagram in figure 2.5, where the Josephson junction is modeled as a parallel circuit of an ideal Josephson contact, a resistance R_n , a capacitance C , and a noise source I_f . Due to its geometry, the Josephson junction has a capacitance of

$$C = \epsilon_0 \epsilon_r \frac{A}{d} \quad (2.18)$$

where ϵ_0 is the vacuum permittivity, ϵ_r the dielectric constant of the barrier material as well as A and d the area and thickness of the barrier. This results in a displacement current

$$I_d = C \frac{dU}{dt} \quad (2.19)$$

if the junction voltage changes over time. The fluctuation current is composed of various contributions, such as thermal noise [Nyq28a] with a spectral power density of

$$S_I(f) = \frac{4k_B T}{R_n} \quad (2.20)$$

and $1/f$ noise, which dominates at low frequencies, typically below about 1 kHz. Adding these four current contributions together and using Kirchhoff's current law, we get the total current

$$I = I_s + I_n + I_d + I_f \quad (2.21)$$

through the Josephson junction.

Inserting the first Josephson equation (2.9) and the second Josephson equation (2.11) into (2.21), we can express the total current with the time- and phase difference-dependent nonlinear differential equation

$$I = I_c \sin(\varphi) + \frac{1}{R_n} \frac{\Phi_0}{2\pi} \frac{d\varphi}{dt} + C \frac{\Phi_0}{2\pi} \frac{d^2\varphi}{dt^2} + I_f \quad (2.22)$$

which describes the dynamic of a Josephson junction. In the RCSJ model, we assume the resistance the normal resistance R_n from chapter 2.2.2, being constant in temperature and voltage. Additionally we neglect the fluctuation current I_f for the following discussion.

Tilted Washboard Potential To get a more intuitive equation, we use the Josephson coupling energy

$$E_{J0} = \frac{\hbar I_c}{2e} \quad (2.23)$$

of the junction, which results from the overlap of the two macroscopic wave functions of the superconducting electrodes [Jos65] and with the normalized total current $i = I/I_c$ we arrive at the analytically solvable differential equation

$$\left(\frac{\hbar}{2e}\right)^2 C \frac{d^2\varphi}{dt^2} + \left(\frac{\hbar}{2e}\right)^2 \frac{1}{R_n} \frac{d\varphi}{dt} + \frac{d\varphi}{dt} \{E_{J0}[1 - \cos \varphi - i\varphi]\} = 0. \quad (2.24)$$

Defining the terms of equation (2.24) as

$$M = \left(\frac{\hbar}{2e}\right)^2 C \quad (2.25)$$

$$\eta = \left(\frac{\hbar}{2e}\right)^2 \frac{1}{R_n} \quad (2.26)$$

$$U = E_{J0}[1 - \cos \varphi - i\varphi] \quad (2.27)$$

we get the differential equation of a particle with mass M and damping η , in the potential U . This brings us to the depiction of the tilted washboard potential as seen in figure 2.6 with the tilt of the potential being proportional to the reduced current i . Up to $I < I_c$ the potential has local minima and the phase particle can stay in a stable position. For $I > I_c$ there are no local minima and the phase particle can slide down the potential where the constant movement of the particle is equivalent to the constant time evolution of the phase difference φ . The capacity C of the junction correlates to the driving force of the particle and the resistance R correlates inverse to the damping which we will discuss more detailed in the following section.

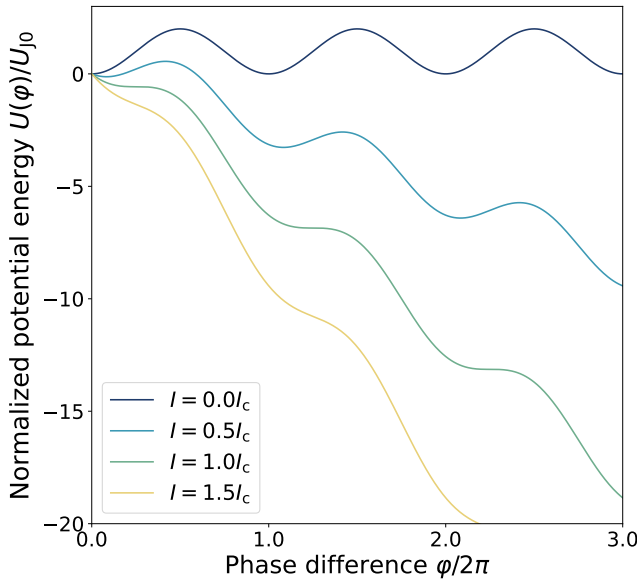


Figure 2.6: Plot of the normalized washboard potential $U(\varphi)/U_{J0}$ for various values of the normalized current $i = I/I_c$. For $0 < i < 1$, there exist local minima, at $i = 1$, saddle points, and for $i > 1$, there are no local extreme points.

Damping and IV-characteristic To understand the damping of the phase particle, we are looking at strong and weakly damped Josephson junctions. A measure for the damping of the junction is the Stewart-McCumber parameter

$$\beta_C = \frac{2e}{\hbar} I_c R_n^2 C. \quad (2.28)$$

In the case of a strongly damped potential ($\beta_C \ll 1$), which correlates to a small resistor connected in parallel to the junction, a so-called shunt resistance, the *IV*-characteristic is the same if the current starts from zero and increases over I_c or if the current is bigger than the critical current and decreases until it is smaller than I_c . This effect occurs due to the strong damping where the particle is able to be stopped in local minima again, if the damping is big compared to the mass which correlates

to the inertia of the particle as well as here to the capacitance of the junction. For weakly damped junctions ($\beta_C \gg 1$), if the current is bigger than I_c , the particle will continue to slide down the potential when reducing the current even below I_c , because the damping is weaker than the kinetic energy. The IV -characteristic for increasing current is the same as for strongly damped junctions.

2.3 Superconducting Quantum Interference Devices

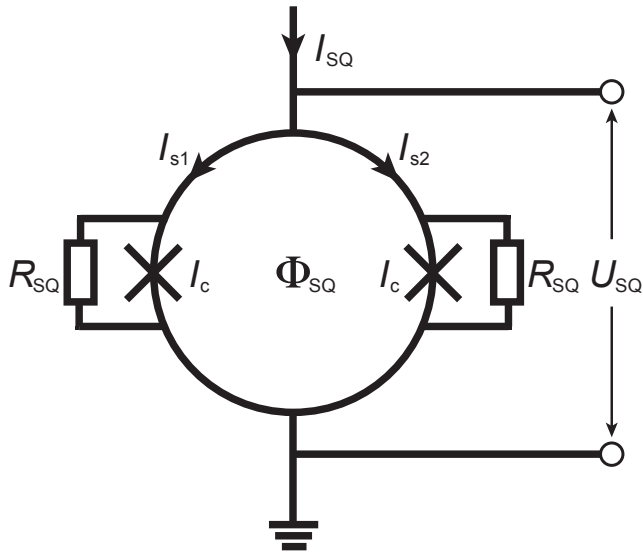


Figure 2.7: Schematic representation of a dc-SQUID. Sketched is a superconducting loop interrupted by two identical Josephson junctions connected in parallel, each with critical currents I_c . The loop has an inductance of L_{SQ} and encloses the magnetic flux Φ_{SQ} . Additionally, the junctions are shunted with identical resistors R_{SQ} to suppress hysteretic behavior in the IV -characteristics. The SQUID is operated with a bias current I_{SQ} , and the voltage drop across it is labeled as U_{SQ} .

SQUIDs¹ are highly sensitive magnetometers which measure a change $\Delta\Phi$ in magnetic flux over a broad frequency spectrum and with low intrinsic noise contribution. The working principle is based on flux quantization and the Josephson effect which we discussed in sections 2.1 and 2.2. While individual Josephson junctions can be used to measure magnetic flux changes, their sensitivity depends on the area penetrated by the external magnetic field, consequently junctions with a thickness of a few micrometers can only resolve magnetic fields with flux densities in the range of a few mT. In order to achieve a resolution of magnetic flux densities in the range of a few μT or even nT, the area penetrated by the magnetic flux needs to be increased, for which a dc-SQUID can be used. As depicted in figure 2.7, a dc-SQUID consists of a superconducting loop with inductance L_{SQ} , which is fed by a current I_{SQ} and interrupted by two parallel and identical Josephson junctions, each with critical currents I_c . In this case, the relevant area is not just the junction area but the cross-sectional area of the ring. Typically, each Josephson junction is shunted with a resistor to

¹Superconducting Quantum Interference Devices

prevent hysteresis on the IV -characteristic [Cla04a]. In the following we will discuss the geometry and operating principle of a dc-SQUID.

2.3.1 Zero Voltage State

In this section we discuss the SQUID in the case where $U_{\text{SQ}} = 0$ and $I_{\text{SQ}} < 2I_c$. By assuming identical Josephson junctions connected in parallel, the supercurrent flowing through the SQUID is determined by the relationship

$$I_{\text{s,SQ}} = I_c \sin \varphi_1 + I_c \sin \varphi_2 = 2I_c \cos \left(\frac{\varphi_1 - \varphi_2}{2} \right) \sin \left(\frac{\varphi_1 + \varphi_2}{2} \right) \quad (2.29)$$

through Kirchhoff's current law and the first Josephson equation. By choosing an integration path deep inside the SQUID loop and considering that the change in phase ϕ of the macroscopic wave functions Ψ along the closed path within the conductor loop can only be integer multiples of 2π , we obtain according to [Cla04b] the expression for the gauge-invariant phase differences

$$\varphi_2 - \varphi_1 = \frac{2\pi\Phi_{\text{SQ}}}{\Phi_0} \quad (2.30)$$

of the two junctions, where Φ_{SQ} is the magnetic flux through the superconducting loop. Substituting this result into equation (2.29), we obtain the flux-dependent supercurrent

$$I_{\text{s,SQ}} = 2I_c \cos \left(\pi \frac{\Phi_{\text{SQ}}}{\Phi_0} \right) \sin \left(\varphi_1 + \pi \frac{\Phi_{\text{SQ}}}{\Phi_0} \right). \quad (2.31)$$

The total magnetic flux

$$\Phi_{\text{SQ}} = \Phi_{\text{ext}} + \Phi_{\text{cir}} \quad (2.32)$$

in the SQUID is composed of an externally applied flux Φ_{ext} and a flux $\Phi_{\text{cir}} = L_{\text{SQ}}I_{\text{cir}}$ generated by the shielding current $I_{\text{cir}} = (I_{\text{s1}} + I_{\text{s2}})/2$ due to flux quantization. This results in the expression

$$\Phi_{\text{SQ}} = \Phi_{\text{ext}} - L_{\text{SQ}}I_c \sin \left(\pi \frac{\Phi}{\Phi_0} \right) \cos \left(\varphi_1 + \pi \frac{\Phi}{\Phi_0} \right), \quad (2.33)$$

which, together with Equation (2.31), forms a system of equations that can be used to describe the characteristics of a dc-SQUID. To analyze limiting cases, we introduce the screening parameter

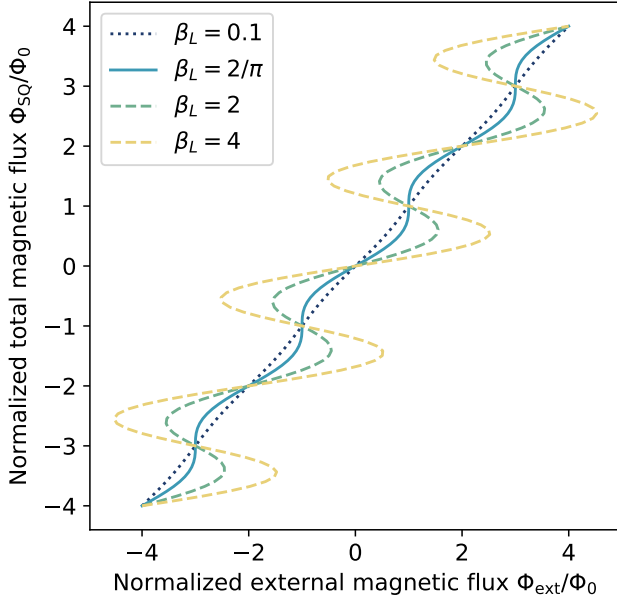


Figure 2.8: Variation of the normalized total magnetic flux Φ_{SQ}/Φ_0 with respect to the externally applied magnetic flux Φ_{ext}/Φ_0 for different values of the screening parameter β_L . Hysteretic behavior is observed for $\beta_L > 2/\pi$, indicated by a dashed line. The limiting case of $\beta_L = 2/\pi$ is marked with a solid line, and non-hysteretic behavior with a dotted line.

$$\beta_L = \frac{2L_{\text{SQ}}I_c}{\Phi_0} \quad (2.34)$$

which represents the ratio of the magnetic flux generated by the maximum possible circulating current $I_{\text{cir},m} = I_c$ and $\Phi_0/2$.

For the limiting case of small bias currents $I_{\text{SQ}} \ll I_c$, the relationship in equation (2.29) can be expressed as $\sin \varphi_1 \approx -\sin \varphi_1$, simplifying equation (2.33) to

$$\frac{\Phi_{\text{ext}}}{\Phi_0} = \frac{\Phi_s}{\Phi_0} + \frac{\beta_L}{2} \sin \left(\pi \frac{\Phi}{\Phi_0} \right). \quad (2.35)$$

Following equation (2.35), the behavior of the total magnetic flux Φ_{SQ} is depicted as a function of the externally applied flux Φ_{ext} , in Figure 2.8, for various values of β_L . It can be observed that the curve becomes hysteretic for $\beta_L \geq 2\pi$, and consequently the same external flux could generate different values for the total magnetic flux.

In the limit $\beta_L \ll 1$, the expression for the maximum supercurrent, as derived from equation (2.31), becomes

$$I_{s,\text{SQ}}^{\max} \approx 2I_c \left| \cos \left(\pi \frac{\Phi_{\text{ext}}}{\Phi_0} \right) \right| \quad (2.36)$$

because the total flux in the SQUID is then solely determined by the externally applied flux. For $\beta_L \gg 1$, the ring current circulating in the SQUID loop is much

larger than a flux quantum and is therefore approximately quantized:

$$\Phi_{\text{cir}} = \Phi_{\text{SQ}} - \Phi_{\text{ext}} \approx n\Phi_0. \quad (2.37)$$

From this, it can be inferred that in this case, the modulation of the supercurrent ΔI_s by the external magnetic field significantly decreases with increasing shielding parameter and follows approximately $I_c/I_{\text{cir}}^{\max} \propto 1/\beta_L$ [Cla04c].

2.3.2 Voltage State

Practical SQUIDs are operated in the voltage state, at a constant bias current above the maximum supercurrent $I_{s,\text{SQ}}^{\max}$. If the maximum supercurrent is exceeded, additional quasiparticle currents flow through the SQUID, leading to a finite voltage drop. In the limit of small shielding currents ($\beta_L \ll 1$) and strong damping through low-resistive shunt resistors ($\beta_C \ll 1$), the equation

$$\langle U(t) \rangle = I_c R_n \sqrt{\left(\frac{I_{\text{SQ}}}{2I_c} \right)^2 - \left[\cos \left(\pi \frac{\Phi_{\text{ext}}}{\Phi_0} \right) \right]^2} \quad (2.38)$$

represents the average voltage drop across the SQUID [Cla04b]. The behaviour of the *IV*-characteristics in this case is similar to that of a single overdamped Josephson junction. However, for such a SQUID, relatively large magnetic fields are required due to the small area penetrated by magnetic flux, making it rather impractical. Numerical simulations demonstrate that the optimal energy sensitivity (see 2.3.4) of a dc-SQUID can be achieved for $\beta_L \approx 1$ and $\beta_C \approx 1$ [Tes77]. In the general description of a dc-SQUID, it is necessary to additionally consider the capacitance C and fluctuating noise currents I_f of the Josephson junctions, as well as the inductance L_{SQ} of the SQUID loop. In this general case, the dc-SQUID can be described by a set of time-dependent nonlinear equations which can be solved numerically [Tes77, Bru82, DW84].

2.3.3 Characteristic Parameters

In this section, we discuss the behavior and important parameters of a dc-SQUID with negligible shielding currents ($\beta_L \ll 1$) and overdamped Josephson junctions ($\beta_C \ll 1$). Since the operation of an optimal SQUID ($\beta_L \approx 1, \beta_C \approx 1$) follows an analogous pattern, the insights discussed here can be directly applied to it. SQUIDs are typically operated in the voltage state by applying a bias current $I > 2I_c$ or bias voltage U_{SQ} [Dru04]. As a result, a periodic output signal is generated as a function of the external magnetic flux. Figure 2.9 shows the characteristics of a

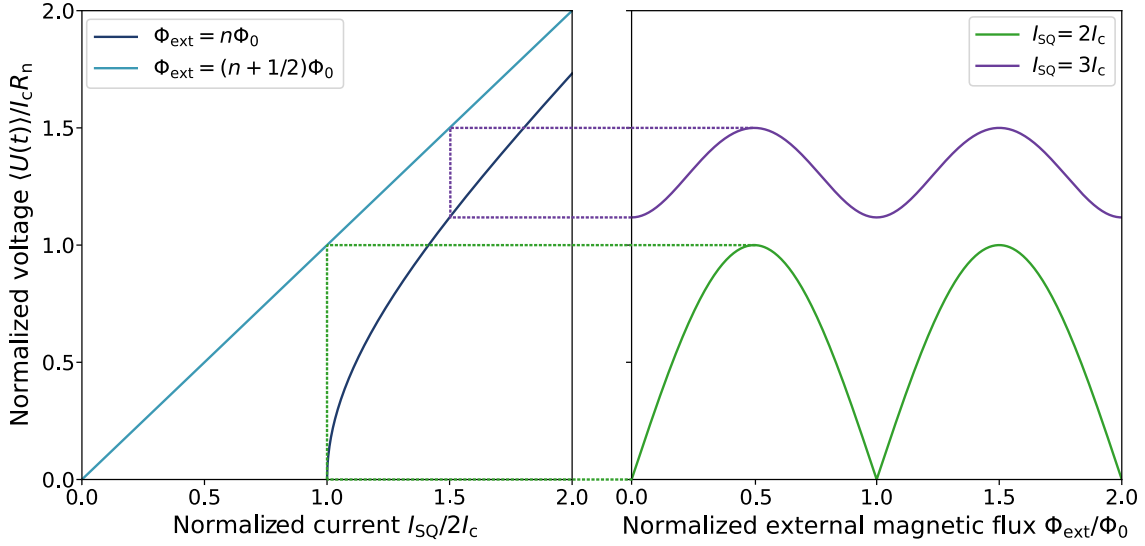


Figure 2.9: Characteristics of a dc-SQUID with negligible shielding currents and over-damped Josephson junctions. Left: *IV*-characteristics at external magnetic fluxes that are integer and half-integer multiples of a magnetic flux quantum. Right: Corresponding voltage-flux characteristic at different constant bias currents.

dc-SQUID which is operated with a bias current. On the left side the two extreme cases $\Phi_{ext} = n\Phi_0$ and $\Phi_{ext} = (n + 1/2)\Phi_0$ of the *IV*-characteristics are displayed, with the curves for all other values of Φ_{ext} lying between these two. On the right side the corresponding voltage-flux characteristic for the two exemplary values of $I_{SQ} = 2I_c$ and $I_{SQ} = 3I_c$ are shown. The flux-voltage characteristic has the largest amplitude ΔU_{SQ} for $I_{SQ}^{\max} = 2I_c$ and has a theoretical maximum of $\Delta U_{SQ}^{\max} = 2I_c R_n$, as can be seen in figure 2.9. Thus, the dc-SQUID functions as a highly sensitive flux-to-voltage converter (bias voltage mode) or flux-to-current converter (bias current mode). The highest sensitivity is observed at the working point which is the steepest point of the flux-voltage characteristic or the flux-current characteristic. For the optimal SQUID this would be at a flux bias of $(2n + 1)\Phi_0/4$. By applying an appropriate flux offset, the working point is chosen in such a way that the flux to voltage transfer coefficient

$$V_\Phi = \left| \left(\frac{\partial U_{SQ}}{\partial \Phi_{ext}} \right)_{I_{SQ}=\text{const.}} \right| \quad (2.39)$$

as well as the flux to current transfer coefficient

$$I_\Phi = \left| \left(\frac{\partial I_{SQ}}{\partial \Phi_{ext}} \right)_{U_{SQ}=\text{const.}} \right| \quad (2.40)$$

are maximized. The resistance of the SQUID is a dynamic resistance

$$R_{\text{dyn}} = \frac{\partial U_{\text{SQ}}}{\partial I_{\text{SQ}}} = \frac{V_{\Phi}}{I_{\Phi}} \quad (2.41)$$

and is dependent on the bias current or bias voltage and the chosen working point [Cla04d].

2.3.4 SQUID Noise

According to the fluctuation-dissipation theorem [Nyg28b] every ohmic resistor R generates thermal voltage noise with a constant power spectral density $S_V(f) = 4k_B T R$ across a wide frequency range. Neglecting additional noise contributions, the voltage noise of a dc-SQUID is given by [Can96]

$$S_V(f) = \frac{4k_B T L_{\text{SQ}} V_{\Phi}^2}{2R_{\text{SQ}}} + 4k_B T R_{\text{dyn}}, \quad (2.42)$$

of which the first term is due to the circulating current and the second one due to thermal voltage fluctuations across the SQUID. Numerical simulations have shown that equation (2.42) simplifies to

$$S_V(f) \approx 18k_B T R. \quad (2.43)$$

for $\beta_L = 1$. [Tes77, Bru82].

Using the flux-to-voltage coefficient V_{Φ} the voltage noise can be converted into the intrinsic flux noise

$$\sqrt{S_{\Phi}(f)} = \frac{\sqrt{S_V(f)}}{V_{\Phi}} \quad (2.44)$$

which is a characteristic quantity to determine the resolution of a SQUID.

Another contribution to the overall noise is the $1/f$ -noise which increases towards low frequencies, the causes of which are not fully understood [Tes82, Koc07, Wel10, Dru10, Ant13, Kum16, Wan18].

Thus, the spectral power density of the overall intrinsic flux noise is given by the phenomenological equation

$$S_{\Phi} = S_{\Phi,w} + \frac{S_{\Phi,1/f}(1 \text{ Hz})}{(f/\text{Hz})^{\alpha}} \quad (2.45)$$

with values for α between 0.5 and 1 [Dru10, Kem16], where $S_{\Phi,w}$ describes the frequency independent white noise contribution and $S_{\Phi,1/f}(1 \text{ Hz})$ the frequency dependent $1/f$ -noise at 1 Hz.

3. Experimental Methods

In this chapter, the operations of the utilized two-stage setup, as well as the measurement setups and methods for determining the characteristics and parameters of the SQUID array, the first-stage SQUID, and the two-stage setup, will be explained.

3.1 Operation of dc-SQUIDs

3.1.1 Linearization of the dc-SQUID Signal

A dc-SQUID, as described in section 2.3.3, exhibits a flux-voltage or flux-current characteristic that is periodic with respect to Φ_0 . Due to the periodicity of this characteristic, the output signal does not vary linearly with the external magnetic flux, and magnetic flux changes $\Delta\Phi_{\text{SQ}}$ bigger than about $\Phi_0/4$ can not be accurately quantified. To achieve a linear output signal over a bigger range for magnetic flux changes, a flux feedback technique, so called flux-locked loop (fll), as depicted in figure 3.1 and described in [Che04], is employed. To achieve the optimal working point as described above, and illustrated in figure 3.1, the bias current I_{SQ} through the SQUID and a current I_Φ through a feedback coil which is inductively coupled to the SQUID via the mutual inductance

$$M_f = \frac{\Delta\Phi_{\text{SQ}}}{\Delta I_f}, \quad (3.1)$$

are adjusted. The inductive coupling is generally described by the mutual inductance, which describes the relationship between the magnetic flux induced in one coil by the rate of change of current in another coil. In this and the following description, it is taken into account that the input of the differential room temperature amplifier is highly resistive, and practically no current flows into its input. When the input coil induces magnetic flux within the SQUID as $\Phi_{\text{SQ}} = I_i M_i$, the resulting voltage drop across the SQUID U_{SQ} is compared by a differential room temperature amplifier with a offset voltage U_b that corresponds to the SQUID's working point. The deviation of the voltage across the SQUID from the offset voltage is then amplified by the factor A , integrated and fed back into the SQUID via a feedback resistor R_f and a feedback coil with the mutual inductance M_f as compensation flux

$$\Phi_f = M_f I_f = M_f \frac{A(U_{\text{SQ}} - U_b)}{R_f} \sim \Phi_i. \quad (3.2)$$

This process keeps the magnetic flux within the SQUID constant, thereby keeping the SQUID at the working point. The initial flux signal within the SQUID can be determined using the output voltage $U_{\text{out}} = \Delta\Phi_{\text{SQ}} A R_f / M_f$, which drops across the feedback resistor. In such a SQUID setup with a room-temperature amplifier, the spectral power density of the apparent flux noise of the SQUID is given by

$$S_\Phi = S_{\Phi,\text{SQ}} + \frac{S_{U,\text{rta}}}{V_\Phi^2} + \frac{S_{I,\text{rta}}}{I_\Phi^2} + S_{I,\Phi} M_f^2. \quad (3.3)$$

In this context, $\sqrt{S_{\Phi,\text{SQ}}}$ represents the intrinsic noise of the SQUID as well as $\sqrt{S_{U,\text{rta}}}$ and $\sqrt{S_{I,\text{rta}}}$ the voltage and current noise of the room-temperature amplifier and the noise of the current source for the flux bias of the SQUID $\sqrt{S_{I,\Phi}}$. In the course of this work, the low-noise and wideband SQUID electronics XXF-1 from Magnicon GmbH was used, which provides all the necessary current and voltage sources, as well as room-temperature amplifier and feedback circuits. The noise of the current source $\sqrt{S_{I,\Phi}}$ for the flux bias, was determined in the work of [Kaa20] to be $\sqrt{S_{I,\Phi}} \approx 2.4 \text{ pA}/\sqrt{\text{Hz}}$ for white noise and $\sqrt{S_{I,\Phi}} \approx 10 \text{ pA}/\sqrt{\text{Hz}}$ for the $1/f$ -noise with an exponent of $\alpha \approx 1.22$. The noise values of the room temperature amplifier of the SQUID electronics are provided in [Dru06] with $\sqrt{S_{U,\text{rta}}} \approx 0.33 \text{ nV}/\sqrt{\text{Hz}}$ and $\sqrt{S_{I,\text{rta}}} \approx 2.6 \text{ pA}/\sqrt{\text{Hz}}$. For a single dc-SQUID with typical transfer coefficients of $V_\Phi \approx 50 \mu\text{V}/\Phi_0$ and $I_\Phi \approx 20 \mu\text{A}/\Phi_0$, the voltage noise is calculated to be $\sqrt{S_{U,\text{rta}}} = 6.6 \mu\Phi_0/\sqrt{\text{Hz}}$, and the current noise is $\sqrt{S_{I,\text{rta}}} = 0.13 \mu\Phi_0/\sqrt{\text{Hz}}$. Hence, the amplifier's current noise can typically be neglected. However, the total apparent flux noise of the amplifier is substantially higher than the intrinsic flux noise of a SQUID, which typically falls in the range of $1 - 5 \mu\Phi_0/\sqrt{\text{Hz}}$. To address this issue, it is feasible to interpose a low-noise cryogenic amplifier between the SQUID and the room-temperature electronics, this will be discussed in the following section.

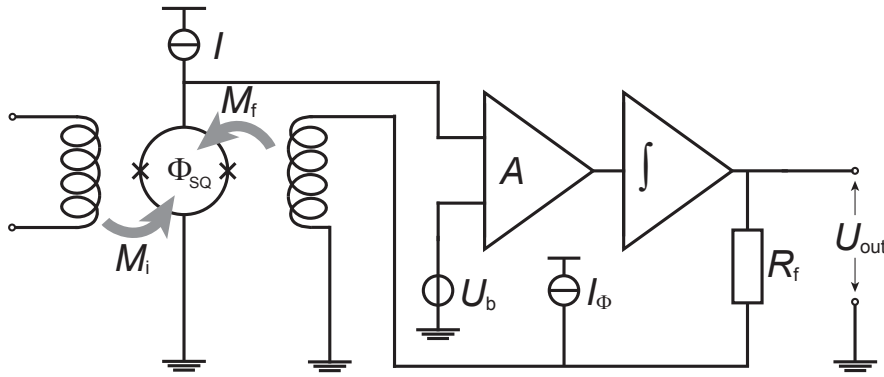


Figure 3.1: Schematic representation of a single-stage operated dc-SQUID, where the SQUID signal is linearized using flux feedback.

3.1.2 Two-Stage Setup

In the setup discussed above, the overall noise is typically limited by the room temperature electronics. To decrease the noise of the system and to increase the transfer coefficients, a second stage SQUID can be introduced as a low noise amplifier for the first stage SQUID. This amplifier SQUID typically is a SQUID array, representing a series connection of N individual dc-SQUID cells, thereby exhibiting an N -fold larger voltage swing and a larger flux-to-voltage coefficient V_Φ . In figure 3.2, the implementation of such a two-stage SQUID setup with flux feedback is illustrated schematically. Therefore, a gain resistor R_g is connected in parallel to the first-stage SQUID, with a value significantly smaller than the dynamic resistance of the SQUID $R_{\text{dyn},\text{SQ}}$ at its working point. By applying a constant operating current I , the voltage across the SQUID is adjusted to remain nearly constant, thus corresponding to the voltage bias mode discussed in section 2.3.3. This minimizes the power dissipated

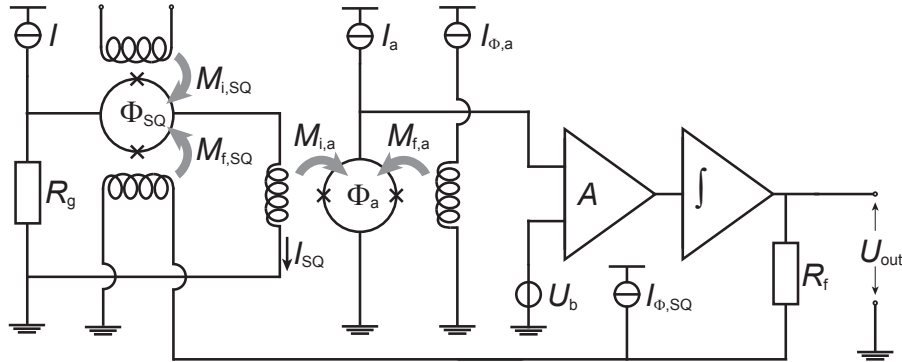


Figure 3.2: Schematic representation of a two-stage dc-SQUID setup where the output signal of the first-stage dc-SQUID is amplified by a second dc-SQUID array. On the left side is the first-stage SQUID, with the input and feedback coil, along with the gain resistor used to generate the voltage bias. In the middle is the SQUID array, which serves as an amplifier for the first-stage SQUID, along with the array feedback coil and the array input coil, the latter of which originates from the first-stage SQUID. On the right side is the room temperature differential amplifier, along with the feedback resistor.

in the first-stage SQUID, what can be understood through the relation for electrical power $P = U \cdot I$. In figure 2.9 it can be seen that for the current bias with maximum voltage swing, a greater power P is dissipated than for a small voltage bias, where the current swing is greatest. $I_{\Phi,\text{SQ}}$ is used to maintain the first-stage SQUID at its optimal working point, as described earlier. A flux change in the first-stage SQUID is generated through an input coil with mutual inductance $M_{i,\text{SQ}}$, typically originating from a detector. The current I_{SQ} through the SQUID depends periodically on the flux Φ_{SQ} in the SQUID and couples into the amplifier SQUID array via a coil with mutual inductance $M_{i,a}$, where it is read out as described earlier in section 3.1.1. The

SQUID array operates in the current bias mode and is maintained at the optimal working point using the bias current I_a and the current $I_{\Phi,a}$, which induces a flux offset into the SQUID array through a feedback coil with mutual inductance $M_{f,a}$.

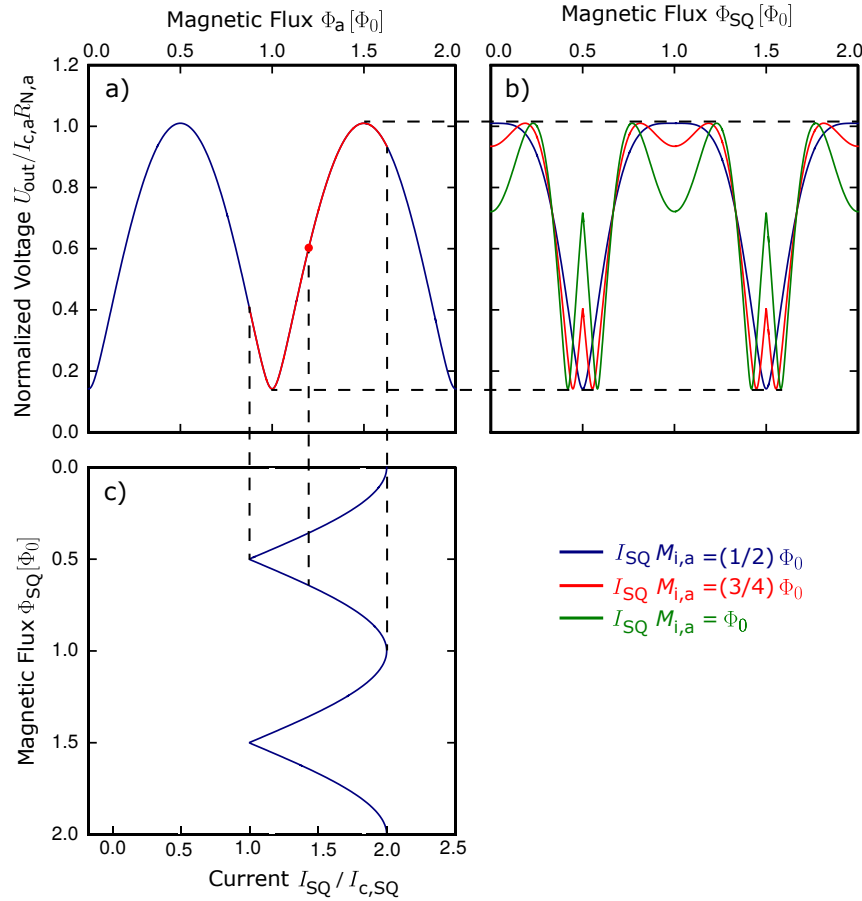


Figure 3.3: Characteristics of the two-stage setup, adapted from the work of [Fer15]. Of that: c) The current flowing through the first-stage SQUID as a function of the magnetic flux Φ_{sq} . a) The voltage drop across the SQUID array as a function of the magnetic flux Φ_a and in red for the case $I_{\text{sq}} M_{i,a} = (3/4)\Phi_0$. b) The voltage drop across the SQUID array as a function of the magnetic flux in the first-stage SQUID Φ_{sq} for different values of $I_{\text{sq}} M_{i,a}$.

The linearization is performed as described earlier, through the feedback coil of the first-stage SQUID with mutual inductance $M_{f,\text{sq}}$, where the initial flux change is compensated, and the working point of the overall characteristic of the two-stage setup is kept constant.

Figure 3.3 displays the flux-voltage characteristic of the two-stage setup. Of this, figure 3.3 c) shows the current I_{sq} flowing through the first-stage SQUID, which

corresponds to the current in the input coil $M_{i,a}$ of the secondary SQUID, in dependence of the magnetic flux in the primary SQUID Φ_{SQ} . According to the equation $\Phi_a = I_{SQ}M_{i,a}$, a magnetic flux induced by the current through the first-stage SQUID is coupled into the SQUID array. The flux-voltage characteristic of the SQUID array is depicted in 3.3 a). In this way the first-stage SQUID modulates, as indicated in red, the voltage edges of the array through the current I_{SQ} and the resulting magnetic flux in the SQUID array Φ_a . In Figure 3.3 b), the resulting flux-voltage characteristic of the two-stage setup is shown for different values of magnetic flux change in the SQUID array. The characteristic corresponds to the voltage drop across the SQUID array as a function of the magnetic flux in the first-stage SQUID. If the current change ΔI_{SQ} generates magnetic flux change $\Delta I_{SQ}M_{i,a} > \Phi_0/2$ through the input coil of the SQUID array, then the maximum of the two-stage characteristic splits into two maxima, and the minimum into two minima. When the magnetic flux is $\Delta I_{SQ}M_{i,a} > \Phi_0$, it is not possible to find an explicit working point [Dru96b]. In such a two-stage SQUID, the flux-to-flux coupling

$$G_\Phi = \frac{\partial\Phi_{SQ}}{\partial\Phi_a} = \frac{M_{i,a}}{R_{dyn,SQ}} V_{\Phi,SQ} = I_{\phi,SQ} M_{i,a} \quad (3.4)$$

describes the ratio of the change in magnetic flux in the SQUID array to that in the first-stage SQUID.

The intrinsic flux noise of the two-stage setup

$$S_\Phi = S_{\Phi,S} + \frac{S_{\Phi,a}}{G_\Phi^2} + \frac{S_{U,rtta}}{G_\Phi^2 V_\Phi^2} + \frac{S_{I,rtta}}{G_\Phi^2 I_\Phi^2} + \frac{S_{I,\Phi_a} M_{f,a}^2}{G_\Phi^2} + \frac{4k_B T R_g}{G_\Phi^2 (R_g + R_{dyn})^2} M_{i,a}^2 \quad (3.5)$$

is composed of the intrinsic noise of the first-stage SQUID $\sqrt{S_{\Phi,SQ}}$, the intrinsic noise of the SQUID array $\sqrt{S_{\Phi,a}}$, the voltage noise $\sqrt{S_{V,rtta}}$ and the current noise $\sqrt{S_{I,rtta}}$ of the room-temperature amplifier, the noise of the current source for the flux bias of the SQUID array $\sqrt{S_{I,\Phi_a}}$ and the current noise caused by the gain resistance R_g . Except for the intrinsic noise of the first-stage SQUID, all the mentioned noise contributions can be reduced by the flux-to-flux coupling factor G_Φ .

3.2 Experimental Setup

The majority of the measurements carried out in this work took place at a temperature of 4.2 K, well below the critical temperature of $T_c = 9.2$ K for high-purity bulk Nb material [Car90]. For this purpose, the SQUID chips were glued onto a circuit board using GE Varnish and electrically connected using aluminum bonding wires.

The circuit board with the chip to be measured was mounted on the sample holder of a dipstick. However, this has not been executed yet. This probe was immersed in a transport container filled with liquid helium for the measurements. The sample holder was shielded by a soft-magnetic Cryoperm shield as well as a superconducting Nb shield to minimize the influence of external magnetic fields. The wiring of the setup is realized using twisted CuNi wires, which were soldered to the circuit board and terminate at a 24-pole LEMO connector at the upper end of the dipstick. To generate constant bias currents, periodic signal currents, and for reading the SQUID response, a SQUID electronics of type XXF-1¹ was used. During the measurement, both current-voltage and flux-voltage characteristics were recorded, using a KEYSIGHT InfiniiVision DSO-X 2004A oscilloscope².

The noise measurements took place at a temperature of 10 mK in a ³He/⁴He-dilution refrigerator BF-LD250 from BlueFors³. The operation of ³He/⁴He-dilution refrigerators is explained in [Ens05b]. For the noise measurement, the chips were glued to a circuit board using GE Varnish and electrically connected using aluminum bonding wires. To enhance thermalization, a large gold pad is available on the chip (see Chapter 4), on which a thermal contact could be established to the circuit board via gold bonds. The circuit board has the shape of long "fingers", to allow for especially good magnetic shielding [Kaa20]. During the measurement, each finger of the board was inside a 112 mm long and 15 mm wide tube made of niobium, manufactured from solid material with a wall thickness of 4.4 mm. These tubes served as superconducting shielding, thus ensuring the suppression of external magnetic fields. The circuit board was fixed to a copper experimental holder, which was directly mounted on the experimental platform, ensuring good thermal coupling. The three-finger circuit board was connected via two 30-pin connector sockets. As in the dipstick experiments, the SQUIDs were operated and read out using the XXF-1 electronics from Magnicon. For noise measurements a dedicated setup was used based on the USB-6361 analog-to-digital-converter⁴. As the sampling rate of this ADC is limited to 500 kHz, an additional low-pass filter with a cut-off frequency of 100 kHz was used to prevent aliasing effects [Sha49]. Additionally a home-made battery-powered amplification stage with a tenfold amplification was added between low-pass and digitizer.

¹Magnicon GmbH, Barkhausenweg 11, 22339 Hamburg, Germany

²Keysight Technologies GmbH, Herrenberger Strasse 130, 71034 Böblingen, Germany

³BlueFors Cryogenics Oy, Arinatie, 00370 Helsinki, Finnland

⁴National Instruments Germany GmbH, Ganghoferstraße 70b 80339 München

3.3 Characterization

To analyze the dc-SQUID array, the first-stage SQUID is not operated, so that there is no current flowing through the first-stage SQUID and no external magnetic flux coupled into it. In the following, the subscripts Ib and Ub indicate current bias and voltage bias, respectively. The current sensitivity $1/M_{f,a}$ of the feedback coil of the array was determined by analyzing the periodicity of the flux-voltage characteristics with respect to the current in the coil. There is no direct way to measure the current sensitivity $1/M_{i,a}$ of the input coil of the dc-SQUID array, but as it shares the same geometrical layout as the feedback coil, we assume $1/M_{i,a} = 1/M_{f,a}$.

To record the current-voltage characteristic of the array, the bias current I_a was introduced as a generator signal, and the voltage across the array was measured for the two extremes of the IV -characteristic, $(n + 1/2)\Phi_0$ and $n\Phi_0$. The flux coupling into the array was adjusted using the feedback coil. The resistance R_N in the normal conducting state of the array could be extracted from the current-voltage characteristics. To record the flux-voltage characteristic, of the SQUID array, the bias current I_a^{\max} which produces the maximal voltage swing ΔU_a^{\max} was applied, this will be described as the operating mode in the following. Then a generator signal was sent through the feedback coil of the SQUID array, and the response was recorded. To optimize the array performance in amplifying the first-stage signal, the working point has to be set. Therefore, an offset voltage V_b was set at the input of the room temperature differential amplifier (typically around half the value of the maximum voltage swing), so that the output signal U_{out} is centered around zero voltage. Additionally a flux bias was set with the feedback coil such that the flux-voltage characteristics of the array is at the working point.

The first-stage SQUID current-voltage characteristic and the current sensitivity $1/M_{i,SQ}$ of the input coil and $1/M_{f,SQ}$ of the feedback coil are recorded similarly as for the array, while using the array in FLL mode to operate as a linear amplifier. As the current and voltage across the first-stage SQUID cannot be directly determined due to the voltage bias, they were reverse-calculated using the equations $I_{SQ} = U_{\text{out}}/R_{f,a}$ and $U_{SQ} = R_g(I - I_{SQ})$. To put the first-stage SQUID in operating mode, a bias voltage is generated by the current I and the gain resistance R_g .

The critical current of the individual Josephson Junctions could be calculated for the first-stage SQUID and the SQUID array through the relation [Vos81, Dru96a]

$$I_c \approx \frac{I_{\text{lb}}^{\max}}{2} + \frac{k_B T}{\Phi_0} \left(1 + \sqrt{1 + \frac{I_{\text{lb}}^{\max}}{k_B T / \Phi_0}} \right) \quad (3.6)$$

by determining the current I_{lb}^{\max} for which the voltage swing of the flux-voltage char-

acteristics is maximized. For all measurements discussed so far, a periodic triangular generator signal was used, while for the characterization of the transfer coefficients and the coupling factor we used a periodic square generator signal. To determine the flux-to-voltage transfer coefficient $V_{\Phi,a}$ and the flux-to-current transfer coefficient $I_{\Phi,a}$ of the array, it was operated with flux feedback, and the change in output voltage was measured in response to a small test signal superimposed on the constant bias current I_a or offset voltage V_b . The flux-to-voltage transfer coefficient $V_{\Phi,t}$ and flux-to-current transfer coefficient $I_{\Phi,t}$ of the two-stage setup were measured analogously.

To measure the flux-to-flux transfer coefficient G_Φ of the two-stage setup, a voltage bias was applied to the first-stage SQUID which resulted in the maximum output signal U_{out}^{\max} . Then a small generator signal was applied to the feedback coil of the array and the flux feedback was operated on the first-stage SQUID and the response was recorded at the output of the two-stage setup.

Measurements of the flux noise were conducted for the two-stage setup, and for the array alone. For the two-stage noise measurement, the array and first-stage SQUID are in operating mode and no generator signal is applied. The flux feedback is locked on the first-stage SQUID. Measuring the noise of the array alone follows the same principle, only with the first-stage SQUID not operating and flux feedback locked on the array.

4. Design of the Two-Stage SQUID

In the framework of this thesis, a new two-stage setup was designed and fabricated in the institute's cleanroom. The design is based on a dc-SQUID, which functions as the first-stage SQUID, as well as a second-stage dc-SQUID array as a low-noise amplifier. The first-stage SQUID is based on the work of [Kah24], while the dc-SQUID array is based on the work of [Kem15]. In the following, the design of the integrated setup will be discussed. The constrain for the design, was to match the bonding scheme of similar chips¹ which are already used for the AMoRE experiment. As a result, the length of the signal line from the first-stage SQUID to the dc-SQUID array is decreased, and shorter signal propagation times are achieved, which lead to an increased readout bandwidth. A major challenge of an integrated setup is the relatively large intrinsic power dissipation, which we try to tackle by specific thermalization structures [Maz24].

4.1 First-Stage SQUID

Figure 4.1 schematically depicts the first-stage SQUID which is used in the integrated setup. The SQUID is realized as a second-order parallel gradiometer, consisting of four oval-shaped washer loops connected in parallel and located in a lower Nb-layer. As a result of the parallelly connected washer loops, the total inductance of the washer is 1/4 of the inductance of a single loop and has a design value of $L_{SQ} = 147 \text{ pH}$. This value was determined within the research group [Bau22] and adopted during the development of the 6nH first-stage SQUID [Kah24], which is used here. The washer loops of the previous design were 5 μm wide to support a single turn input and feedback coil. The design used in this work has a two-turn input coil to increase its inductance to $L_i = 6 \text{ nH}$. Therefore the washer was widened from 5 μm to 10 μm , at the position where it couples to the input coil to provide enough space. To compensate for the wider washer part, the size of the washer hole was made larger, therefore we expect the inductance L_{SQ} of the washer to be approximately the same. To avoid magnetic flux trapping in form of vortices, the maximum width W of the superconducting structures was determined with the relation

$$B_v^{\text{crit}} = 1.65 \frac{\Phi_0}{W^2}, \quad (4.1)$$

¹Typ C73 from PTB, Berlin

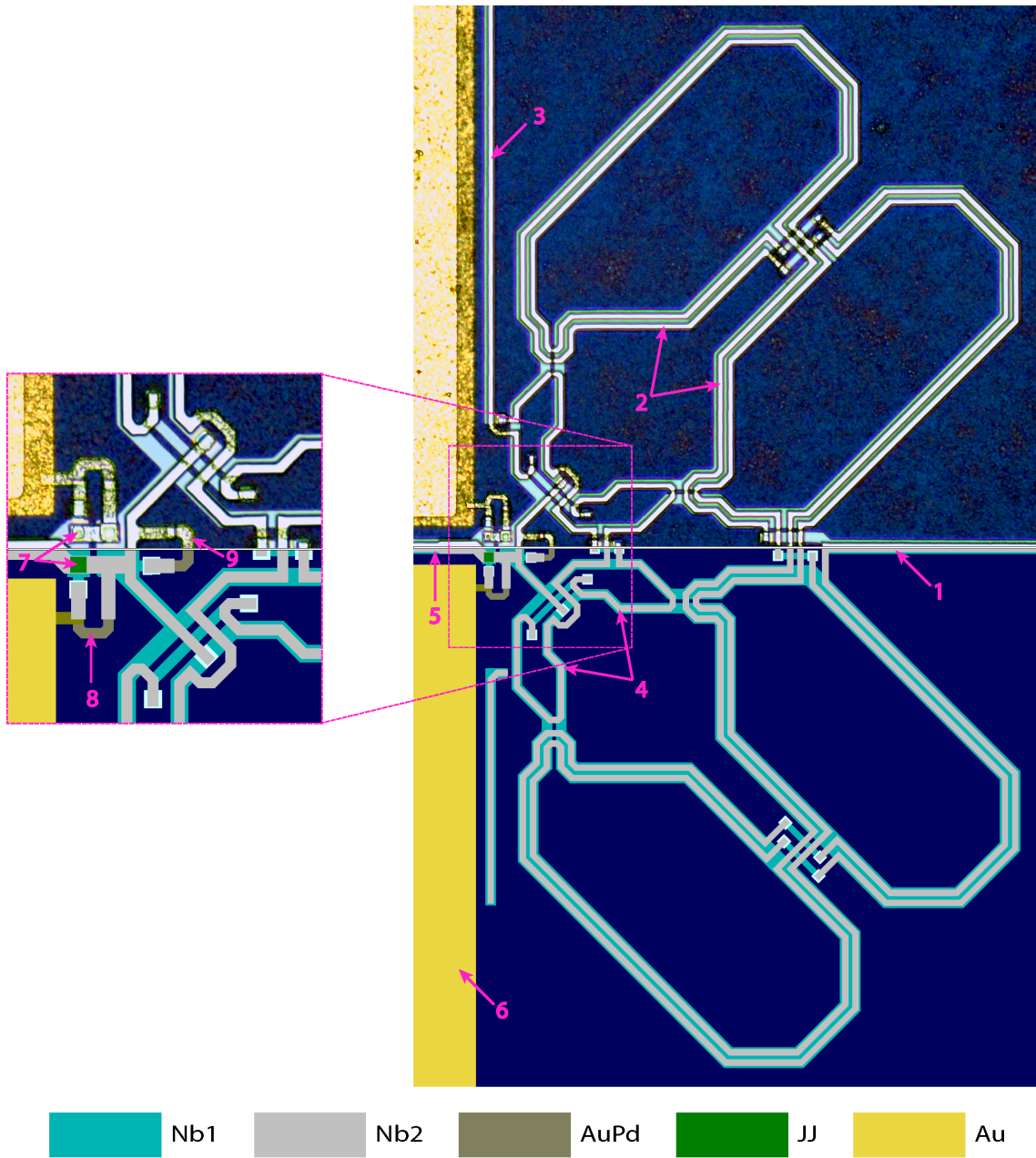


Figure 4.1: Right: First-stage SQUID schematic drawing on the bottom and mirrored image with the use of an optical microscope on top. **Left:** Zoom into the junction area of the first-stage SQUID. The numbers indicate the position of the 1) input coil supply line, 2) input coil, 3) feedback coil supply line, 4) feedback coil, 5) bias current feed, 6) junction heat sinks 7) Josephson junctions, 8) junction shunt resistors , 9) washer shunt resistor.

[Kui08] where B_v^{crit} is the critical external field perpendicular to the current direction and to the width. Assuming a maximal magnitude of the earths magnetic field at its surface of $65 \mu\text{T}$ for, one finds a maximal width of $7.2 \mu\text{m}$, which was increased to $10 \mu\text{m}$ due to magnetic shielding of the setup and mitigating the earths magnetic field. The Nb/Al-AlO_x/Nb Josephson junctions are square-shaped and have a side length of $4.5 \mu\text{m}$ with a targeted critical current $I_c = 6 \mu\text{A}$ and consequently a critical current density of $j_c = 30 \text{ A/cm}^2$. For these junctions, a capacity of $C_{\text{SQ}} = 0.95 \text{ pF}$ was specified in the work of [Bau22]. Each Josephson junction is shunted with a $3 \mu\text{m}$ wide and $14.8 \mu\text{m}$ long AuPd-resistor R_s to prevent hysteretic behavior of the IV-characteristic as discussed in section 2.3. The design value of the junction shunt resistor was calculated by numerically minimizing the extrinsic energy sensitivity ϵ_p , while restricting the Stewart-McCumber parameter and the screening parameter to $\beta_C \leq 0.7$ and $\beta_L \leq 1$, respectively, in order to avoid hysteric behavior of the SQUIDs [Bau22]. The value of $R_s = 6 \Omega$ was then adopted for the first-stage SQUID used in this work. Therefore with Ohm's circuit law we expect the normal resistance of one dc-SQUID to be $R_N = 3.0 \Omega$.

For effective cooling and consequently reduced thermal noise, each of these shunts is connected to a large heat sink made of gold. The heat sink consists of two layers, out of which the lower layer is sputtered, and the upper layer is electroplated. To dampen the $L_{\text{SQ}}C_p$ resonance, which is caused by the washer inductance and the parasitic capacity C_p , attributable to the geometric arrangement of the washer and input coil and is further explained in [Fab18], the washer is shunted with an AuPd-resistor R_d . The washer shunt has the same dimensions as the junction shunt resistors, to minimize current noise caused by R_d [Enp86, Ryh92]. With this values the Stewart-McCumber parameter and the screening parameter calculate to $\beta_c = 0.62$ and $\beta_L = 0.85$ according to equation 2.28 and 2.34.

The flux-generating input and feedback coils are structured as second-order serial gradiometers in the second Nb-layer and are electrically isolated from the washer by a SiO₂ layer. The input coil has two turns per washer loop, with a designed inductance of approximately $L_i = 6 \text{ nH}$, while the feedback coil has one turn per washer loop, with a total total designed inductance of $L_f = 336 \text{ pH}$. Input and feedback coil, have a line width of $3 \mu\text{m}$. To connect the first and second Nb-layer at the desired connection points, $5 \mu\text{m}$ wide squares, with missing isolation layer, are established to form super conducting vias. Another influence to the geometry and form of the washer, input coil and feedback coil, is the maximization of the area where input coil and feedback coil overlap with the washer in constructive winding direction for magnetic induction, while at the same time minimizing crosstalk between the coils.

To optimize the transfer coefficient and flux noise, the dc-SQUID is operated with an asymmetric bias current feed, which is described in detail in [Cla04e]. To mini-

mize asymmetric interference of the dc-SQUID with the external magnetic field, the symmetry of the dc-SQUID was maximized. For this purpose, dummy structures are placed where needed in the superconducting layers, which are electrically separated from the rest of the dc-SQUID.

4.2 18-cell dc-SQUID Array

In the dc-SQUID array, which is used in the integrated design, 18 single dc-SQUID array cells are connected in series. As part of this thesis, the previously used dc-SQUID array was expanded from 16 to 18 dc-SQUID array cells. The expansion of 2 cells should result in a larger voltage swing, a steeper flux to voltage transfer coefficient, and thus a better signal-to-noise ratio. Figure 4.2 depicts a single cell of the dc-SQUID array which is a first order serial gradiometer. As with the first-stage SQUID, the washer structure of the dc-SQUID array cell is mostly located in the lower Nb-layer. It consists of two square shaped, serially connected loops. Due to the serial connection of the two washer loops, the total inductance of the washer of the dc-SQUID array cell equals the sum of both loops. Each of the square shaped washers is $5\text{ }\mu\text{m}$ wide and the washer hole has a width of $42.5\text{ }\mu\text{m}$. To maximize the area where the washer and input coil or feedback coil overlap, two U-shaped protrusions deviating from the square shape of the washer, are included in the washer design. With a side length of $4\text{ }\mu\text{m}$, the square shaped Nb/Al-AlO_x/Nb Josephson junctions of the dc-SQUID array cell are slightly smaller than the Josephson junctions of the first-stage SQUID. As the critical current density for the array is also given by $j_c = 30\text{ A/cm}^2$, the critical current can be calculated as $I_c = 4.8\text{ }\mu\text{A}$ using the junction size. This is the result of the adjustment to a larger inductance of the dc-SQUID array than that of the dc-SQUID. Both Josephson junctions are shunted with a $30.6\text{ }\mu\text{m}$ long and $5.0\text{ }\mu\text{m}$ wide AuPd-resistor. With a height of 200 nm and a specific sheet resistance of $1.22\Omega/\text{square}$, this results in a resistance of 7.47Ω for each junction shunt resistor. Therefore with Ohm's circuit law we expect the normal resistance of one dc-SQUID array cell to be 3.73Ω and the normal resistance of the 18-cell dc-SQUID array to be $R_N = 67.2\Omega$. For cooling the resistors, each one of them is connected to a AuPd-heatsink, one of which is additionally covered with gold for better heat conduction.

With a width of $3\text{ }\mu\text{m}$, the input and feedback coil are both located in the second Nb-layer and both have two turns per washer. For each coil, only the inner loop is located above the washer, in a manner such that the conductor trace is aligned perfectly with the washer trace center. The outer loop has a constant distance of $2\text{ }\mu\text{m}$ from the washer, as this is the minimum distance all structures are designed to have from each other due to alignment constraints in the fabrication process. To

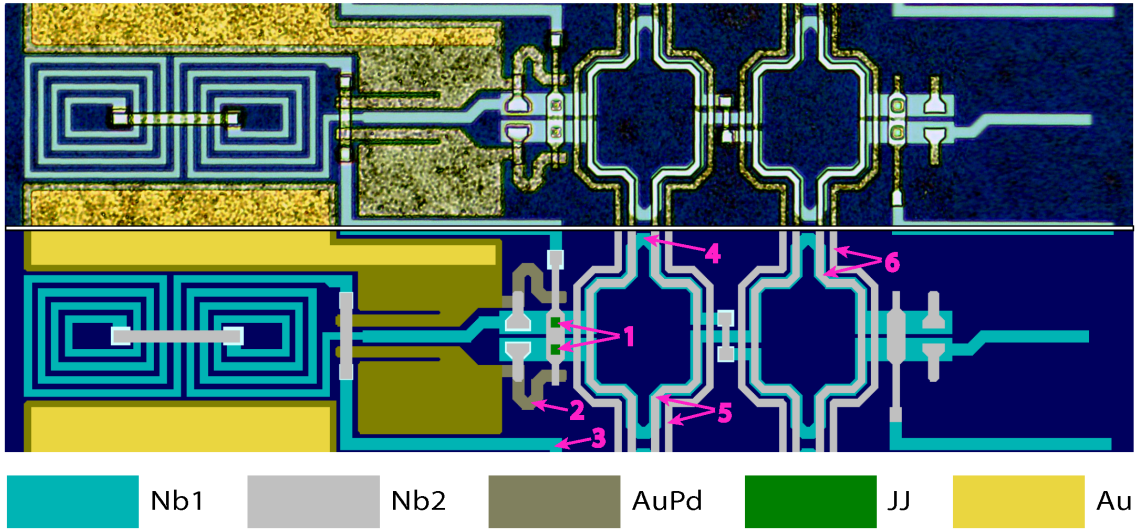


Figure 4.2: Two cells of the dc-SQUID array, as a schematic drawing at the bottom and a mirrored image with the use of an optical microscope on top. The numbers indicate the position of the 1) Josephson junctions, 2) shunt resistors, 3) bias current feed, 4) washer, 5) input coil, 6) feedback coil

maximize the flux to current transfer coefficient I_Φ , the current feed of the array is designed maximally asymmetric and thus minimizes the influence of the current noise of the room temperature electronics. Each current injection of the dc-SQUID array cells is preceded by a filter coil, to remove high frequency noise from the current source. To maximize the symmetry of the dc-SQUID array, dummy structures were placed opposite to the junctions, in the first and second Nb-layer. For the same purpose, at both ends of the array, two dummy cells are added. These dummy cells differ from the real cells, only in the fact that the two Josephson junctions are missing or are replaced with a via to conduct the electrical bias current further to the washer of the next array cell.

4.3 Integrated Two-Stage Design

The integrated two stage design, which is shown as a schematic drawing in figure 4.3, is microfabricated twice on a single $3\text{ mm} \times 3\text{ mm}$ silicon substrate. Located near the bottom edge of the chip is the $45\text{ }\mu\text{m}$ long and $150\text{ }\mu\text{m}$ wide gain resistor R_g which has a design resistance of about $370\text{ m}\Omega$. According to the equation for electrical power $P = U^2/R$, the gain resistor experiences significantly higher power dissipation compared to the first-stage SQUID, as they both have the same voltage drop, but the gain resistor has a significantly lower resistance. To minimize heat transfer from

the gain resistor to the dc-SQUID, they are placed far apart from each other and additionally, for better heat dissipation, the gain resistor is connected to a large gold heat sink. Another large gold heat sink is located in the upper part of the integrated design, which is not electrically connected to any other structure. It can be used for better thermalization of the chip to a copper experiment holder via bonding wires made of gold.

A determining factor of the design is the bond pad layout, which was adapted to the specific requirements of size and positions for AMoRE. To reduce parasitic inductance, all connections to the first-stage SQUID are made in a stripline geometry. The supply and return lines, for the bias current and signal lines, are right upon each other and are separated by an isolation layer. In the stripline geometry, the lower Nb-line has a width of $5\text{ }\mu\text{m}$ and the second Nb-line a width of $3\text{ }\mu\text{m}$, to prevent fabrication errors due to misalignment. The input coil of the first-stage SQUID is connected to the $\pm\text{IN}$ bond pads on the right-hand side with an R_xC_x -damping element, from the work of [Bau22], in parallel. In the R_xC_x element, a resistor $R_x = 17.6\text{ }\Omega$ is connected in parallel to the input coil, to dampen the resonance caused by the inductance of the input coil and the parasitic capacitance C_p , arising from the geometry of the SQUID washer and input coil. Additionally a capacitance $C_x = 10\text{ pF}$ is connected in series to the resistor R_x to prevent low-frequency current noise from the shunt resistor R_x being fed into the input coil. The $-\text{IN}$ bond pad is duplicated to match the current bond pad layout of our MMCs. This gradiometric bonding scheme helps to reduce interference signals during data acquisition, which are caused by external magnetic fields and mechanical vibrations of the bond wires, by a factor of approximately one order of magnitude [Sch19]. The bias current supply of the first-stage SQUID, the feedback coil of the array and the bias current supply of the array, share one common ground bond pad. The three grounds were combined due to restrictions on the number of wires inside the cryostat. The $+\text{FX}$ bond pad connects to the feedback coil at the upper left-hand side of the dc-SQUID array, which then connects to the shared $-\text{VIFX}$ ground bond pad, with the power line realized in the upper Nb-layer. For supporting the dc-SQUID array with a bias current, the $+\text{V}$ bond pad connects through a power line in the lower Nb-layer to the current feed on the lower right-hand side of the dc-SQUID array.

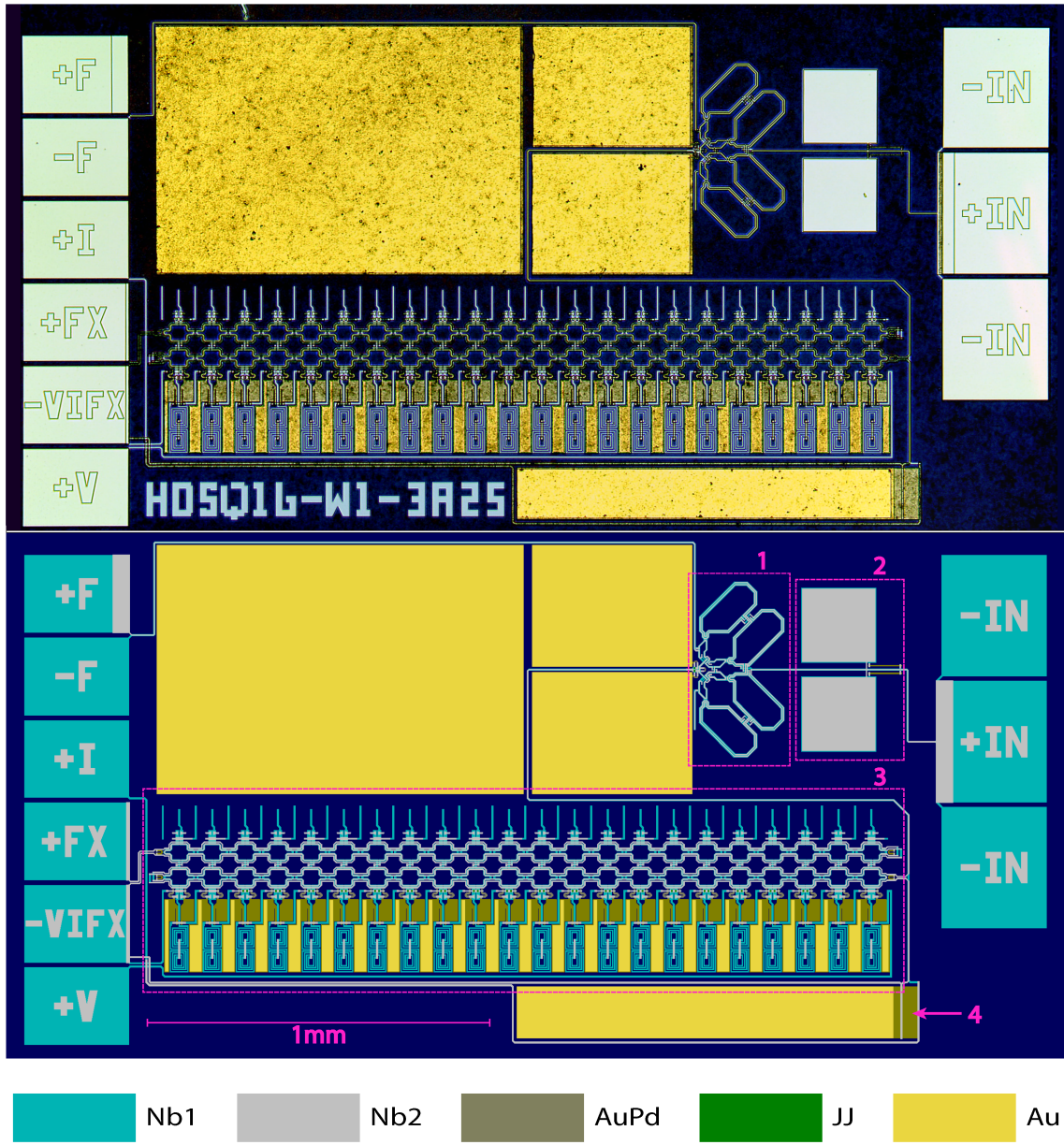


Figure 4.3: Chip on which the integrated two-stage SQUIDs are microfabricated, as a schematic drawing at the bottom and a mirrored image with the use of an optical microscope on top. For the purpose of providing a sense of measurement, a scale is placed on the bottom left side. The numbers indicate the position of the 1) first-stage SQUID, 2) RC-filter, 3) dc-SQUID array, 4) gain resistor.

5. Experimental Results

As part of this work, several SQUIDS with the design discussed in chapter 4 were tested at a temperature of $T = 4.2\text{ K}$. Among them, the chip HDSQ16-W1-3C05 was extensively characterized. In addition, the noise of a chip was investigated at $T = 10\text{ mK}$. In the following, the plots and results of these characterizations are summarized. The step structure in the recorded characteristics is caused by artefacts of the measurement setup. First, the results of the individual characterization of the dc-SQUID array and the first-stage dc-SQUID in the two-stage setup at 4.2 K are presented. At the end of the chapter, the flux noise of the two-stage setup is discussed.

5.1 Characterization of the 18-Cell dc-SQUID Array

In the context of this work, an 18-cell dc-SQUID array was characterized at a temperature of $T = 4.2\text{ K}$ as a low-temperature amplifier in the two-stage setup. Therefore the first-stage SQUID was turned off by setting its bias current to zero.

5.1.1 *I/V*-Characteristics of the SQUID Array

In figure 5.1, the current-voltage characteristic of the SQUID array is shown for the two extreme flux states $\Phi_a = n\Phi_0$ and $\Phi_a = (n + 1/2)\Phi_0$. The most relevant parameters measured during the characterization of the SQUID array are summarized in table 5.1. The normal resistance $R_N = 68\Omega$ was read from the current-voltage characteristic, which fits very well to the design value of 67Ω . Through the normal resistance of the array, which is dominated by the two shunt resistors, the sheet resistance of the AuPd-shunts was determined to be $1.23\Omega/\text{square}$, which corresponds closely to the design value of $1.22\Omega/\text{square}$. The critical current, of a single Josephson junction I_c , was calculated from the measured values of the operating current I_{lb}^{\max} at maximum voltage swing $\Delta U_{\text{lb}}^{\max}$, using equation (3.6). This value is $I_c = 4.71\mu\text{A}$, and thus, the critical current density is $j_c = 29.4\mu\text{A}/\text{cm}^2$, representing a deviation of 1.9 % for both values from the design values. The theoretical maximum current swing, which is the maximum current swing for $T = 0\text{ K}$ without thermal smoothening of the characteristics, was estimated to $\Delta I_{\text{Ub},\text{theo}}^{\max} = 3.6\mu\text{A}$ from the current-voltage characteristics. According to [Tes77], the shielding parameter β_L can be experimentally determined by normalizing the theoretical maximum current swing to twice the critical current of the SQUID as $\Delta I_{\text{Ub},\text{theo}}^{\max}/2I_c$. This resulted in a

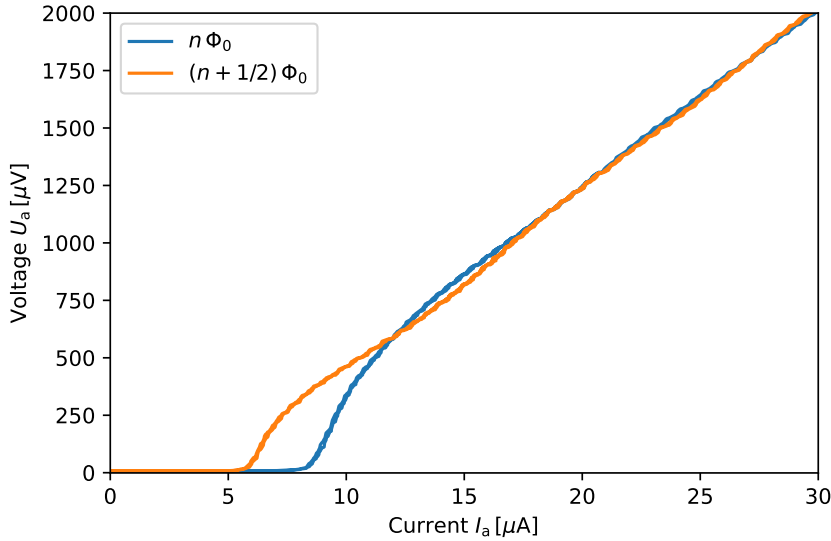


Figure 5.1: Current-voltage characteristics of the 18-cell dc-SQUID array in the two-stage setup at 4.2 K. Plotted is the bias current through the array against the voltage drop across it for two extreme cases of the magnetic flux coupled into the array. The orange curve represents the characteristics for half-integer flux quanta, and the blue one for integer flux quanta. Clearly visible is the zero voltage state up to $5.2 \mu\text{A}$ and $7.4 \mu\text{A}$, the flux sensitive state in which the array operates, and the normal-conducting state where the two characteristics approach a linear dependence above $15 \mu\text{A}$.

shielding parameter $\beta_L = 1.43$. With this value for β_L , the inductance for the array is calculated to be $L_a = 314 \text{ pH}$, corresponding to a value of $L_{a,1} = 17.4 \text{ pH}$ for a single cell. As the Josephson junctions of the first-stage SQUID and the SQUID array are fabricated in the same layer, we can assume a permittivity ϵ and identical layer thickness d . Thereby the capacitance of the SQUID array junctions could be estimated to $C_a = 0.75 \text{ pF}$, using the formula for the capacitance $C = \epsilon A/d$ and the ratio of the areas A of the junctions. Therefore a junction capacitance 0.95 pF for the first-stage SQUID was assumed based on the design value from [Bau22]. With these values, the Stewart-McCumber parameter was determined to be $\beta_C = 0.17$ which ensures a non hysteretic I/V -characteristic, since it is significantly smaller than 1. As there are no recent simulations available for the SQUID array, a comparison will be made with simulations of a previous 16-cell dc-SQUID array utilizing the same array cells, from the work of [Kaa20], upon which the present design is based. In this work the parameters were determined to $\beta_L = 1.31$, $\beta_c = 0.26$ and a washer inductance of $L_a = 285 \text{ pH}$ which corresponds to a single cell inductance of $L_{a,1} = 17.8 \text{ pH}$. While the inductance of the washer is very close to the simulation, β_L is slightly higher and β_c slightly lower.

	I_{lb}^{\max} [μA]	R_N [Ω]	$\Delta I_{\text{Ub},\text{theo}}^{\max}$ [$\mu\text{A}/$]	I_c [μA]	β_L	β_C	$L_{a,1}$ [pH]
Values	8.4	68	3.6	4.71	1.43	0.17	17.4
Design		67		4.80	1.31*	0.26*	17.8*

Table 5.1: Overview of the characteristic parameters of the SQUID array obtained experimentally from the current-voltage characteristic in the two-stage setup. The values marked with * are reference values from a 16-cell dc-SQUID array in the work of [Kaa20], on which the 18-cell dc-SQUID array used in this work is based on. The value $L_{a,1}$ describes the washer inductance for a single cell.

5.1.2 Φ/V -Characteristics of the SQUID Array

The flux-voltage characteristic of the SQUID array shown in figure 5.2 correlates to picture *a*) in figure 3.3. It was recorded at the operating current I_{lb}^{\max} , where the voltage swing ΔU_{lb} is maximal and exhibits a periodic, approximately sinusoidal shape. The most relevant parameters experimentally determined are summarized in table 5.2. From the Φ/V -characteristics, the maximum voltage swing at the bias current

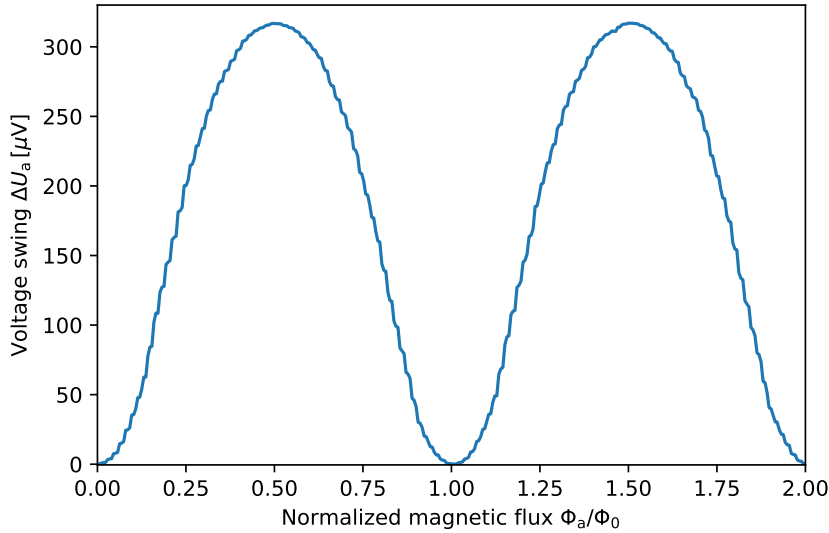


Figure 5.2: Current-voltage characteristics of the 18-cell dc-SQUID array in the two-stage setup.

I_{lb}^{\max} was determined to be $\Delta U_{\text{lb}}^{\max} = 317 \mu\text{V}$. The flux-to-voltage transfer coefficients $V_{\phi}^+ = 1121 \mu\text{V}/\Phi_0$ and $V_{\phi}^- = 1205 \mu\text{V}/\Phi_0$ are similar for positive and negative slopes. The distinct values for the flux-to-current transfer coefficients $I_{\phi}^+ = 13.98 \mu\text{A}/\Phi_0$ and

$I_\phi^- = 4.64 \mu\text{A}/\Phi_0$ for the positive and negative slopes of the flux-voltage characteristic are expected, given that the SQUID array is designed for maximal asymmetric bias current injection. The determination of the reciprocal mutual inductance was carried out by measuring the flux-voltage characteristic and considering the periodicity of the characteristic with the magnetic flux quantum. This resulted in a reciprocal mutual inductance of $1/M_{f,a} = 11.63 \mu\text{A}/\Phi_0$ for the feedback coil. The input coil for the array $1/M_{f,i}$, which comes from the first-stage SQUID, cannot be directly measured. However, since it has the same dimensions as the feedback coil, the same value of $1/M_{f,i} = 11.63 \mu\text{A}/\Phi_0$ can be assumed. This assumption is conformed by the maximum critical current modulation of the first-stage SQUID, which is discussed in more detail in section 5.2. The values of the dynamic resistances $R_{\text{dyn}}^+ = 80 \Omega$ and $R_{\text{dyn}}^- = 262 \Omega$ were determined using equation (2.41) with the values of $V_\phi^{+,-}$ and $I_\phi^{+,-}$. The fact that they differ for the positive and negative slope is due to the asymmetric flux-to-current transfer coefficients which are the result of an asymmetric bias current injection.

$\Delta U_{\text{Ib}}^{\text{max}}$ [μV]	V_ϕ^+ [$\mu\text{V}/\Phi_0$]	V_ϕ^- [$\mu\text{V}/\Phi_0$]	I_ϕ^+ [$\mu\text{A}/\Phi_0$]	I_ϕ^- [$\mu\text{A}/\Phi_0$]	R_{dyn}^+ [Ω]	R_{dyn}^- [Ω]	$1/M_{f,a}$ [$\mu\text{A}/\Phi_0$]	$1/M_{i,a}$ [$\mu\text{A}/\Phi_0$]
317	1121	1205	13.98	4.64	80	262	11.63	11.63

Table 5.2: Overview of the characteristic parameters of the SQUID array obtained experimentally from the flux-voltage characteristic in the two-stage setup.

5.2 Characterization of the First-Stage SQUID in the Two-Stage Setup

The characterization of the new first-stage SQUID described in section 4.1 took place in the two-stage operating mode, with the SQUID array serving as a linear low temperature amplifier. Consequently, the values of the first-stage SQUID could not be directly measured but had to be deduced from the output signal of the two-stage setup, as described in section 3.3.

5.2.1 I/V -Characteristics of the First-Stage SQUID

The current-voltage characteristic of the first-stage SQUID, is shown for the two extremes of magnetic flux coupled into it in figure 5.3, with the orange curve repre-

senting the characteristic for half-integer flux quanta, and the blue one for integer flux quanta. The I/V -characteristics could not be measured directly, but was calculated from the output voltage of the two-stage setup and the values of the flux-locked-loop feedback of the SQUID array as well as the generator signal and the value of the gain resistor R_g , as described in section 3.3. The zero voltage state is clearly visible and the voltage state shows the parts of the maximum current swing as well as the maximum voltage swing. The normal resistance could not be determined, since the signal generator for the bias current I_b was even at maximum setting not high enough to drive the first-stage SQUID into the normal-conducting state. The most

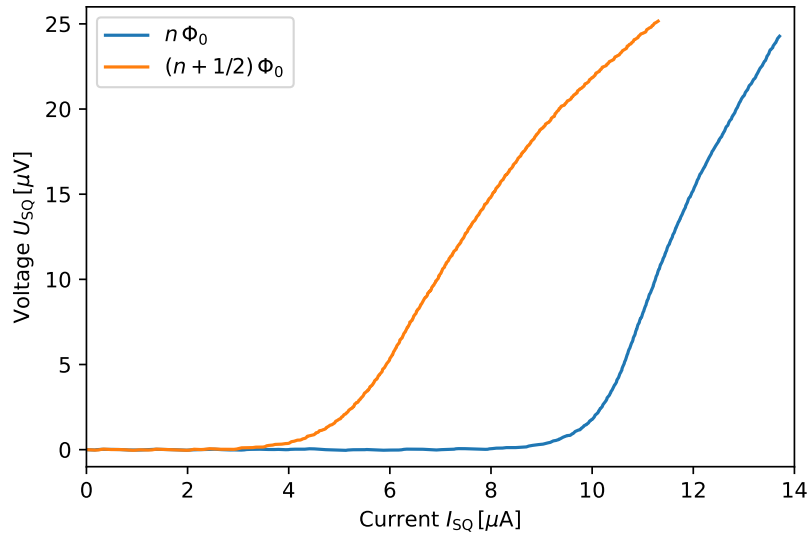


Figure 5.3: Current-voltage characteristics of the first-stage SQUID in the two-stage setup at 4.2 K. Plotted is the current through the first-stage SQUID against the voltage drop across it for the two extremes of the magnetic flux coupled into the first-stage SQUID. The orange curve represents the characteristics for half-integer flux quanta, and the blue one for integer flux quanta.

relevant of the measured properties are summarized in table 5.3. The resistance of the gain resistor was calculated to be $R_g = 367 \text{ m}\Omega$ using the design dimensions of the gain resistor and the AuPd-sheet resistance previously obtained through the normal resistance of the SQUID array. In a similar manner, the normal resistance R_N was calculated to be $R_N = 6.1 \Omega$. This places both resistances very close to the targeted values, as expected from the small deviation of the target value of the SQUID array in section 5.1.1. From the IV -curve the maximum voltage swing and the corresponding operating current were determined to $\Delta U_{Ib}^{\max} = 20.1 \text{ }\mu\text{V}$ and $I_{Ib}^{\max} = 10.0 \text{ }\mu\text{A}$. The latter was then employed, according to Equation 3.6, to calculate the critical current $I_c = 5.56 \text{ }\mu\text{A}$ of a single Josephson junction and consequently

the critical current density $j_c = 27.5 \text{ A/cm}^2$. As the junctions of the SQUID array and first-stage SQUID are manufactured simultaneously, and the critical current density, as described in [Kem13], depends on the pressure and duration of oxygen exposure as $j_c \propto p_{\text{ox}} t_{\text{ox}}$, critical current density j_c of the first-stage SQUID and the SQUID array are expected to be the same. However, due to significant variations in the area of the Josephson junctions during the manufacturing process, the expected value carries a large uncertainty, within which the two critical current densities coincide. This has a small impact on the following parameters. In the same way as in section 5.1.1, the theoretical maximum current swing was estimated to $\Delta I_{\text{Ub},\text{theo}}^{\max} = 5.9 \mu\text{A}$, and from this, the screening parameter was determined to $\beta_L = 0.82$ using the relation $\Delta I_{\text{Ub},\text{theo}}^{\max}/2I_c$, according to [Tes77], therefore being not too far from the optimal value $\beta_L \simeq 1$. Using equation 2.34 and the experimentally determined values for the critical current density and the screening parameter, the inductance of the first-stage SQUID washer was determined to be $L_{\text{SQ}} = 152 \text{ pH}$. The Stewart McCumber parameter was determined to be $\beta_C = 0.60$ by assuming the capacitance of $C = 0.95 \text{ pF}$ for the identically constructed Josephson junctions determined in [Bau22], the normal resistance determined from the AuPd-sheet resistance as well as the critical current determined from the current at the maximum voltage swing with equation 3.6. This ensures a non-hysteretic I/V -characteristics of the first-stage SQUID, since the β_C is well below 1. The three parameters β_L , L_{SQ} and β_C fit well with the design values of $\beta_L = 0.85$, $L_{\text{SQ}} = 147 \text{ pH}$ and $\beta_C = 0.62$.

	$\Delta U_{\text{lb}}^{\max}$ [μV]	I_{lb}^{\max} [μA]	R_N [Ω]	R_g [$\text{m}\Omega$]	$\Delta I_{\text{Ub},\text{theo}}^{\max}$ [μA]	I_c [μA]	β_L	β_C	L_{SQ} [pH]
Value	20.1	10.0	3.2	367	5.9	5.56	0.82	0.60	152
Design			3.0	370		6.00	0.85	0.62	147

Table 5.3: Overview of the characteristic parameters of the first-stage SQUID obtained experimentally from the current-voltage characteristic in the two-stage setup.

5.2.2 $\Phi_{\text{SQ}}/I_{\text{SQ}}$ -Characteristics of the First-Stage SQUID

The first-stage SQUID, is operated in the voltage bias mode, as described in section 3.1.2. The $\Phi_{\text{SQ}}/I_{\text{SQ}}$ -characteristic of the first-stage SQUID, which is shown in figure 5.4, correlates to picture *c*) in figure 3.3. Figure 5.4 shows the current swing of the first-stage SQUID, in dependence of the magnetic flux coupled into it, for the bias voltage which produces the biggest current swing. This is the bias voltage, which is used for operating the two-stage setup, coupling magnetic flux into the SQUID array via the mutual inductance $M_{i,a}$. Therefore, a constant generator current I_b^{\max} was set

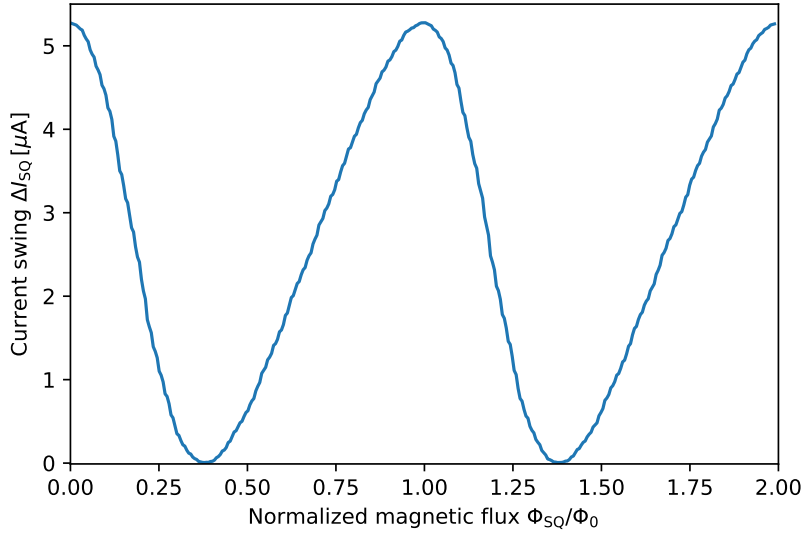


Figure 5.4: Current-voltage characteristic of the first-stage SQUID in the two-stage setup. Plotted is the current swing, as a function of the magnetic flux coupled into the first-stage SQUID.

to create an approximately constant voltage bias using the gain resistor R_g . The most relevant values from this measurement are listed in table 5.4. The maximal current swing was determined from the $\Phi_{\text{SQ}}/I_{\text{SQ}}$ -characteristics to be $\Delta I_{\text{Ub}}^{\max} = 5.3 \mu\text{A}$.

Considering the previously determined reciprocal mutual inductance of $1/M_{i,a} = 11.63 \mu\text{A}/\Phi_0$ of the arrays input coil, it becomes apparent that this value is in good agreement with the maximum voltage swing $\Delta U_{\text{lb}}^{\max} = 317 \mu\text{V}$ of the array, and the maximum voltage swing $\Delta U_{\text{out}}^{\max} = 307 \mu\text{V}$ of the two-stage setup. To utilize the full voltage swing of the array in the two-stage operating mode, as shown in 3.3, the flux change in the array must be at least half a flux quantum induced by the coupling coil. For this, a current change of at least $1/M_{i,a} \cdot \Phi_0/2$, is required. However, since the maximum current swing of the first-stage SQUID is just below this, the maximum voltage swing of the two-stage setup as seen in figure 5.5, is slightly smaller than that of the array.

It can be observed that the $\Phi_{\text{SQ}}/I_{\text{SQ}}$ -characteristics is highly asymmetric, which is the consequence of an asymmetric current I_{SQ} injection. This is intentional to achieve a corresponding asymmetry in the slopes of the Φ/V -characteristics in the two-stage setup, and thus a unilaterally larger flux-to-voltage transfer coefficient V_Φ . How the asymmetry in the current slopes of the first-stage SQUID corresponds to an asymmetry in the slopes of the Φ/V -characteristics in the two-stage setup, through the voltage slopes of the SQUID array, is discussed in section 3.1.2 and shown in figure

3.3. Since the gain resistor R_g generates an approximately constant voltage bias across the first-stage SQUID through the generator current I , the current through it could not be directly varied, as done in the measurement for the array. Consequently the flux-to-current transfer coefficient I_ϕ could not be directly measured, using the oscilloscope as described in section 3.3. Using the Φ/I characteristics of the first-stage SQUID in figure 5.4, the values of the flux-to-current transfer coefficients can be determined to $I_\phi^+ = 10.8 \mu\text{A}/\Phi_0$ and $I_\phi^- = 22.5 \mu\text{A}/\Phi_0$, corresponding to a twice as steep slope of the negative slope compared to the positive one. The reciprocal mutual inductances of the input coil and feedback coil could be determined as described in section 3.3, based on the periodicity of the Φ/I characteristic, to $1/M_{i,\text{SQ}} = 3.47 \mu\text{A}/\Phi_0$ and $1/M_{f,\text{SQ}} = 43.3 \mu\text{A}/\Phi_0$ respectively.

ΔI_{Ub}^{\max} [μA]	I_ϕ^+ [$\mu\text{A}/\Phi_0$]	I_ϕ^- [$\mu\text{A}/\Phi_0$]	$1/M_{f,\text{SQ}}$ [$\mu\text{A}/\Phi_0$]	$1/M_{i,\text{SQ}}$ [$\mu\text{A}/\Phi_0$]
5.3	10.8	22.5	43.3	3.47

Table 5.4: Overview of the characteristic parameters of the first-stage SQUID obtained experimentally from the flux-voltage characteristic in the two-stage setup.

5.3 Integrated Two-Stage Setup

In figure 5.5, the output signal ΔU_{out} of the integrated two-stage setup is shown as a function of the magnetic flux Φ_{SQ} coupled into the first-stage SQUID. It correlates to picture *b*) in figure 3.3. This confirms that the integrated design is functional. The most relevant measured values are summarized in table 5.5. From the Φ/V characteristics, the maximum output voltage swing can be directly determined as $\Delta U_{\text{out}}^{\max} = 307 \mu\text{V}$. It is noteworthy that the maximum voltage swing is smaller than that of the SQUID array. This is because, as described in section 5.2.2, the maximum current swing of the first-stage SQUID cannot fully modulate the voltage slope of the SQUID array. This is further evident in the Φ/V characteristic of the two-stage setup, which lacks double dips at the maxima and minima, as seen in figure 3.3, and instead exhibits an approximately sinusoidal shape. The objective should be to completely modulate the SQUID array however, the modulation of the array should be less than Φ_0 , to ensure that an explicit working point can still be identified. Through the Φ/V -characteristics, as described in section 3.3, the flux-to-voltage transfer coefficients $V_\phi^+ = 2167 \mu\text{V}/\Phi_0$ and $V_\phi^- = 1046 \mu\text{V}/\Phi_0$ as well as the flux-to-current transfer coefficients $I_\phi^+ = 8.67 \mu\text{A}/\Phi_0$ and $I_\phi^- = 4.23 \mu\text{A}/\Phi_0$ of the positive and negative slopes were determined. As designed, the flux-to-voltage

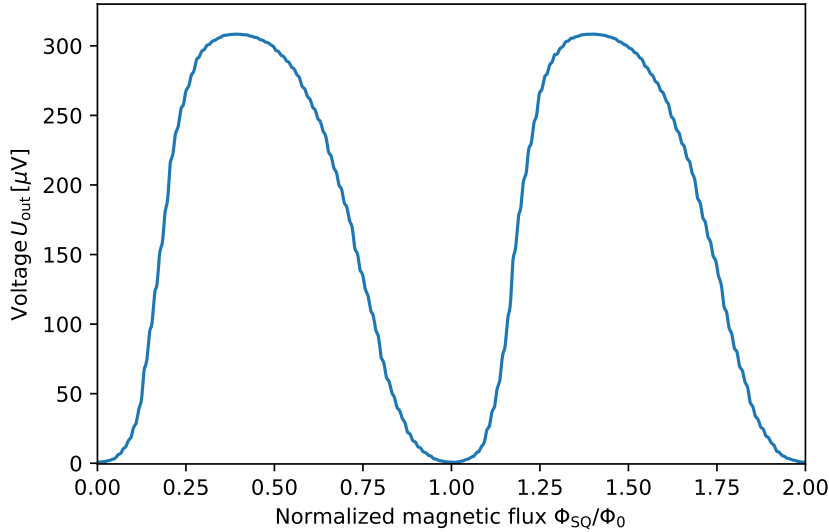


Figure 5.5: Current-voltage characteristic of the two-stage setup. Plotted is the voltage drop across the SQUID array, as a function of the magnetic flux coupled into the first-stage SQUID.

transfer coefficient of one slope is steeper at the expense of the other slope, aiming to maximize the ratio of output signal to magnetic flux coupled into the first-stage SQUID. Thereby it is noticeable that the ratio of the positive and negative slopes of the flux-to-current transfer coefficients $I_{\phi,SQ}^-/I_{\phi,SQ}^+ = 2.08$ of the first-stage SQUID and the flux-to-voltage transfer coefficients $V_{\phi,t}^+/V_{\phi,t}^- = 2.07$ of the two-stage setup are approximately equal. This demonstrates that the steepness of the current slopes of the first-stage SQUID directly transfers to the steepness of the voltage slopes in the two-stage setup.

From the transfer coefficients, the dynamic resistances of the two-stage setup for the positive and negative slopes can be calculated as $R_{\text{dyn}}^+ = 250 \Omega$ and $R_{\text{dyn}}^- = 247 \Omega$. The flux-to-flux coupling G_ϕ was determined as the ratio of a small change in flux in the first-stage SQUID to the resulting change in flux in the SQUID array as described in section 3.3. This resulted in values of $G_\phi^+ = 1.94$ for the positive slope and $G_\phi^- = 0.96$ for the negative slope. For the positive slope, the flux coupled into the SQUID array is almost twice as large as the flux which was initially coupled into the first-stage SQUID, therefore demonstrating the amplifying effect of the overall setup. As a result, the apparent flux noise in the first-stage SQUID can be further reduced as described in equation 3.5.

$\Delta U_{\text{out}}^{\max}$	R_{dyn}^-	R_{dyn}^+	V_ϕ^-	V_ϕ^+	I_ϕ^-	I_ϕ^+	G_ϕ^-	G_ϕ^+
[μV]	[Ω]	[Ω]	[$\mu\text{V}/\Phi_0$]	[$\mu\text{V}/\Phi_0$]	[$\mu\text{A}/\Phi_0$]	[$\mu\text{A}/\Phi_0$]		
307	247	250	1046	2167	4.23	8.67	0.96	1.94

Table 5.5: Overview of the characteristic parameters of the two-stage setup obtained experimentally.

5.4 Noise

The noise measurements of the SQUIDs on chip HDSQ16-W1-3A15, which are presented here, were conducted at a cryostat temperature of $T = 10\text{ mK}$ in a ${}^3\text{He}/{}^4\text{He}$ dilution refrigerator, as described in section 3.2. First we will discuss the noise measurement of the SQUID array only, followed by the measurement of the two-stage setup.

5.4.1 Noise of the SQUID Array

To measure the noise of the SQUID array, it was operated in array only mode with the first-stage SQUID turned off as described in section 3.3. Although the chip was operated at a cryostat temperature of 10 mK , the SQUID itself is significantly warmer due to self-heating. Based on the empirical knowledge of the working group, a temperature of $T = 150\text{ mK}$ for the chip was assumed for this operating mode. The result of this measurement is shown in figure 5.6, where the spectral noise density $\sqrt{S_\Phi}$ is plotted against the frequency. The points of the red curve represent the measured noise data of the SQUID array. At three points, the data from high peaks at 50Hz and multiples, which were coupled in through the power grid, were removed. A cutoff is observed, starting at around 10 kHz , which appears in all measurements and can be traced back to the lowpass filter in the readout chain mentioned in section 3.3. The noise contribution from the gain resistor was determined using equation 2.43 and is indicated by a dashed grey line. The noise contributions from the current noise and voltage noise of the room temperature amplifier of the SQUID electronics were taken from the data set of [Dru06] and are indicated by green and yellow dashed lines. The current noise of the power supply for the feedback coil was taken from [Kaa20] and is indicated by a blue dashed line. From the measurement data, the values for the complete setup including all noise contributions, were determined as $\sqrt{S_{\Phi,w}} = 0.84\text{ }\mu\Phi_0/\sqrt{\text{Hz}}$ and $\sqrt{S_{\Phi,1/f}}(1\text{ Hz}) = 4.2\text{ }\mu\Phi_0/\sqrt{\text{Hz}}$ with $\alpha = 0.9$. Through numerical fitting of equation 2.45, the intrinsic noise contribution of the SQUID array was determined such that, together with all previously mentioned noise contributions, it combines to the data of the noise measurement, according to equation 3.5. In the

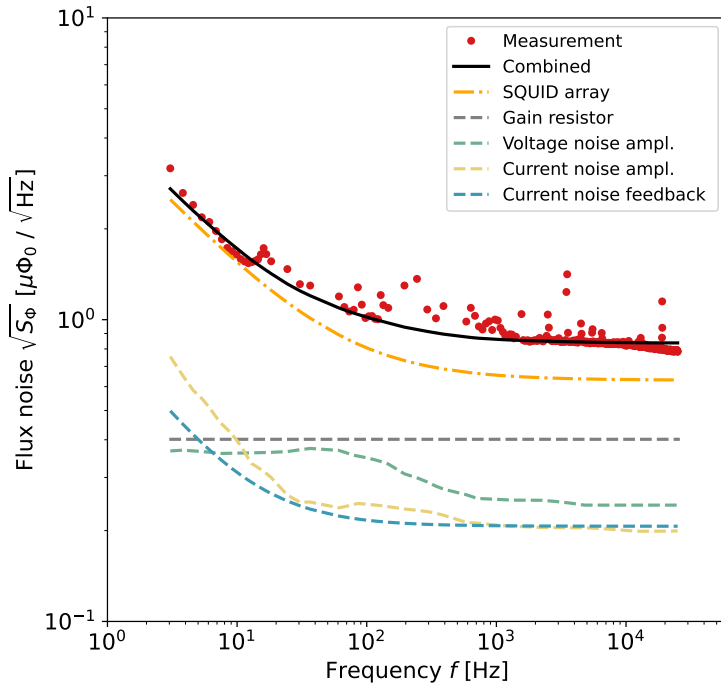


Figure 5.6: Noise spectrum of the SQUID array at a refrigerator temperature of 10 mK. The measured data of the SQUID array noise is shown, where each point represents a recorded data point. The solid line represents the combined data of all noise contributions, while the dash-dotted line represents the numerically determined intrinsic noise of the SQUID array. The dashed lines represent the noise contributions of the SQUID electronics and the gain resistor.

plot, the intrinsic noise of the SQUID array is marked as an orange dash-dotted line and the combined noise contributions as a solid black line. Thereby, the values for the intrinsic noise of the SQUID array were determined to be $\sqrt{S_{\Phi,w}} = 0.63 \mu\Phi_0/\sqrt{\text{Hz}}$ and $\sqrt{S_{\Phi,1/f}}(1 \text{ Hz}) = 4.0 \mu\Phi_0/\sqrt{\text{Hz}}$ with $\alpha = 0.9$, which is comparable to other arrays we produced before [Kem15]. To combine all contributions to the data of the noise measurement, equation 3.5 was modified to correspond to the single-stage SQUID array operation in the two-stage setup. This means that $S_{\Phi,SQ} = 0$, $R_{\text{dyn},SQ} = 0$, and $G_\Phi = 1$,

5.4.2 Noise of the Integrated Two-Stage Setup

Figure 5.7 shows the measured data of the flux noise $\sqrt{S_\Phi}$ of the two-stage setup plotted as red points against the frequency f . Additionally, the aforementioned noise contributions, as well as the previously determined intrinsic flux noise of the SQUID array are indicated in the same way as in section 5.4.1. It is important to

note, that the apparent noise of the array, in terms of flux noise in the first-stage SQUID is now reduced by the flux-to-flux transfer coefficient G_Φ . For this plot, two measurements were conducted, one as described before in section 5.4.1, in the range of 3 Hz – 26 kHz, and another for low frequencies, starting from about 90 mHz. The slight offset in the measurement data of the two-stage setup at approximately 1.5 kHz is caused by different settings of the Gain Bandwidth Product of the SQUID feedback loop during the measurement. Based on the empirical knowledge of the working group, a temperature of $T = 500$ mK for the chip was assumed for the two-stage operating mode. This is significantly higher than in single-stage operating mode, with the vast majority of the temperature increase attributable to power dissipation in the gain resistor. From the measured data, the white noise of the

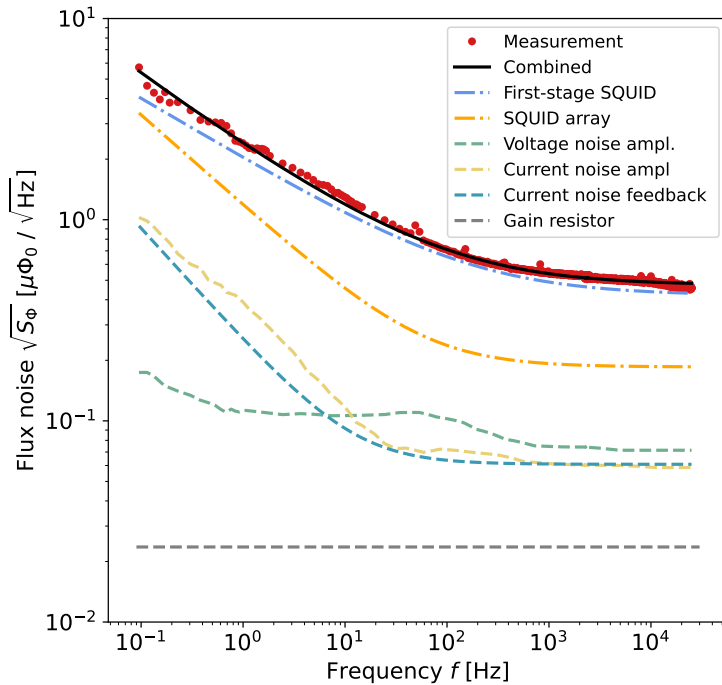


Figure 5.7: Noise spectrum of the integrated two-stage SQUID setup with the first-stage SQUID and a SQUID array as an amplifier at a refrigerator temperature of 10 mK. The measured data of the two-stage noise is shown, where each point represents a recorded data point. The solid line represents the combined data of all noise contributions, while the dash-dotted lines represent the numerically determined intrinsic noise of the SQUID array and first-stage SQUID. The dashed lines represent the noise contributions of the SQUID electronics and the gain resistor.

complete two-stage setup was determined to be $\sqrt{S_{\Phi,w}} = 0.482 \mu\Phi_0/\sqrt{\text{Hz}}$, and the $1/f$ -noise to be $\sqrt{S_{\Phi,1/f}(1 \text{ Hz})} = 2.2 \mu\Phi_0/\sqrt{\text{Hz}}$ with $\alpha = 0.8$. Through numerical fitting of equation 2.45, the intrinsic noise contribution of the first-stage SQUID

was determined such that, together with all previously mentioned noise contributions and the intrinsic noise of the SQUID array, it combines to the data of the noise measurement, according to equation 3.5. Thereby, the values for the intrinsic noise of the first-stage SQUID were determined to be $\sqrt{S_{\Phi,w}} = 0.420 \mu\Phi_0/\sqrt{\text{Hz}}$ and $\sqrt{S_{\Phi,1/f}(1 \text{ Hz})} = 2.0 \mu\Phi_0/\sqrt{\text{Hz}}$ with $\alpha = 0.6$. In the plot, the intrinsic noise of the first-stage SQUID is marked as a light blue dash-dotted line and the combined noise contributions as a solid black line.

The first-stage SQUID clearly dominates the overall noise. This is because the flux-to-flux transfer coefficient G_Φ greatly reduces the noise contributions of the SQUID electronics, as well as the gain resistor R_g and the intrinsic flux noise $S_{\Phi,a}$ of the SQUID array. Consequently, even with the increased temperature in the two-stage operation mode, these contributions are lower than in the single-stage operation. Furthermore, the noise contribution of the gain resistor R_g is largely reduced by the much higher dynamic resistance $R_{\text{dyn},\text{SQ}}$ of the first-stage SQUID. Due to the significantly lower normal resistance $R_{n,\text{SQ}} = 3.2 \Omega$ of the first-stage SQUID compared to the normal resistance $R_{n,a} = 68 \Omega$ of the SQUID array, the intrinsic noise of the first-stage SQUID is lower, even at the higher temperature, compared to the noise of the SQUID array in single-stage operation. Therefore, the overall noise of the two-stage setup is significantly lower than the noise in single-stage operation. The overall noise thus exhibits a low $1/f$ component, and the white noise is comparable to previous two-stage setups, where the first-stage SQUID and SQUID array are housed on separate chips. To further reduce the noise of the integrated two-stage setup, in future operation, a thermal contact could be established via gold bonds on the designated gold surface to a heat sink, thus decreasing the temperature of the chip.

6. Summary and Outlook

In this work, we discuss the development and characterization of an integrated two-stage dc-SQUID for the readout of an MMC-based detector, with particular motivation driven by the constraints of the AMoRE project. In comparison to a two-stage SQUID setup where both stages are distributed on two distinct chips, the length of the signal lines from the first-stage SQUID to the dc-SQUID array is decreased. Therefore shorter signal propagation times are achieved, which leads to an increased readout bandwidth. Additionally, parasitic inductances are reduced due to fewer bonding wires.

The integrated two-stage SQUID contains a first-stage dc-SQUID for the readout of an MMC-based detector and a dc-SQUID array as an amplifier. The input inductance of the first stage SQUID was optimized to a value of 6 nH [Kah24] and the SQUID array was adapted towards 18 cells. Additionally the geometry was adjusted to be compatible with the bonding scheme already employed at AMoRE.

To counteract the heat dissipation of the SQUID array and gain resistor on the chip, the thermal management was improved. To achieve this, the cooling pads for thermalizing the first-stage SQUID were enlarged. Furthermore, an additional layer of gold was applied to the cooling pads of the first-stage SQUID, SQUID array and gain resistor. Additionally, large gold thermalization pads were employed, which allow the thermal anchoring of the chip to the sample holder via gold bonds. The dc-SQUID array was expanded from 16 to 18 cells to increase the voltage swing as well as the flux-to-voltage transfer coefficient.

The characteristic parameters of the SQUID array and the first-stage SQUID were determined at 4.2 K in a liquid helium transport vessel. In this context, we found that the most important parameters of the SQUID array are close to the expected values based on the manufacturing parameters. The first-stage dc-SQUID was investigated in the two-stage operation mode, where the 18-cell dc-SQUID array served as an amplifier. It was demonstrated that the targeted parameters were achieved, and notably, the current swing of the first-stage SQUID adequately modulates the voltage characteristics of the SQUID array. From the characterization of the integrated two-stage setup a flux-to-voltage transfer coefficient of about $V_\Phi = 2170\text{ }\mu\text{V}/\Phi_0$ and a flux-to-flux transfer coefficient of $G_\Phi = 1.94$ were determined. The flux-to-voltage transfer coefficient could be further improved, by increasing the Josephson junction shunt resistances, which could be reached by simultaneously decreasing the Junction capacitance through a manufacturing process known as the cross type process, as described in [Bau22]. This technique is already being further developed within the

research group and is intended to be implemented in future designs.

Furthermore, the integrated two-stage setup was characterized at 10 mK, and its noise, as well as the intrinsic noise of the first-stage SQUID and the SQUID array, were examined. For the SQUID array an intrinsic flux noise of $\sqrt{S_{\Phi,w}} = 0.63 \mu\Phi_0/\sqrt{\text{Hz}}$ for the white noise and $\sqrt{S_{\Phi,1/f}(1\text{Hz})} = 4.0 \mu\Phi_0/\sqrt{\text{Hz}}$ with an exponent $\alpha = 0.9$ for the low-frequency noise contribution was determined in the single-stage operation mode. This is comparable to the flux noise of previous arrays produced within the research group. The first-stage SQUID, exhibits an intrinsic flux noise of $\sqrt{S_{\Phi,w}} = 0.420 \mu\Phi_0/\sqrt{\text{Hz}}$ for the white noise and $\sqrt{S_{\Phi,1/f}(1\text{Hz})} = 2.0 \mu\Phi_0/\sqrt{\text{Hz}}$ with an exponent $\alpha = 0.6$ for the low frequency noise contribution. Furthermore, a flux noise of $\sqrt{S_{\Phi,w}} = 0.482 \mu\Phi_0/\sqrt{\text{Hz}}$ for the white noise and $\sqrt{S_{\Phi,1/f}(1\text{Hz})} = 2.2 \mu\Phi_0/\sqrt{\text{Hz}}$ with an exponent $\alpha = 0.8$ for the low frequency noise contribution of the entire two-stage setup was measured. It was demonstrated that the noise contribution of the first-stage SQUID dominates the overall noise as expected. Therefore, reducing the noise contribution of the first-stage SQUID by decreasing its intrinsic noise, would result in the most significant improvement in the two-stage setup noise. This noise contribution could be improved by optimized cooling, as well as by reducing the capacitance of the Josephson junctions [Bau22].

This characterization demonstrates the successful development of an integrated two-stage setup. Both the flux-to-voltage transfer coefficient and the flux noise are comparable with two-stage setups on distinct chips previously produced within the research group. The flux-to-voltage transfer coefficient could be improved further by a larger mutual inductance of the array input coil and thus stronger modulation of the SQUID array. This could be implemented through a 3-to-1 ratio of the SQUID array feedback coil to the input coil, additionally reducing the flux noise induced by the feedback coil. Another option would be to increase the current swing of the first-stage SQUID, which can be achieved by a larger critical current. This would require reducing the junction capacitance, for example, by using a cross-type process for SQUID fabrication, and concurrently decreasing the washer inductance. However, this would require larger changes in geometry. In future experiments, thermal anchoring of the SQUID chips to the sample holder will further improve the thermalization and thus the noise contributions of especially the first-stage SQUID, which contributes the largest portion of the overall noise will be decreased. Therefore, the integrated two-stage setup is applicable for the AMoRE experiment, which already utilizes chips from the same wafer.

Bibliography

- [And63] P. W. Anderson and J. M. Rowell, Probable observation of the josephson superconducting tunneling effect, *Physical Review Letters*, **10**(6), 230, 1963.
- [Ant13] S. Anton, J. Birenbaum, S. O’Kelley, V. Bolkhovsky, D. A. Braje, G. Fitch, M. Neeley, G. Hilton, H.-M. Cho, K. Irwin, et al., Magnetic flux noise in dc squids: temperature and geometry dependence, *Physical review letters*, **110**(14), 147002, 2013.
- [Bar57] J. Bardeen, L. N. Cooper, and J. R. Schrieffer, Theory of superconductivity, *Physical review*, **108**(5), 1175, 1957.
- [Bau22] F. Bauer, Rauscharme Stromsensor-dc-SQUIDs mit Impedanzanpassung für metallische magnetische Kalorimeter, PhD Thesis, 2022.
- [Bha12] H. Bhang, R. Boiko, D. Chernyak, J. Choi, S. Choi, F. Danevich, K. Efendiev, C. Enss, A. Fleischmann, A. Gangapshev, et al., Amore experiment: a search for neutrinoless double beta decay of ^{100}mo isotope with $^{40}\text{ca}100\text{moo}4$ cryogenic scintillation detector, in *Journal of Physics: Conference Series*, Volume 375, 042023, IOP Publishing, 2012.
- [Bru82] J. Bruines, V. de Waal, and J. Mooij, Comment on:“dc squid: Noise and optimization” by tesche and clarke, *Journal of Low Temperature Physics*, **46**, 383–386, 1982.
- [Buc04] W. Buckel and R. Kleiner, Superconductivity. fundamentals and applications. 2. rev. and enl, 2004.
- [Can96] R. Cantor, Dc squids: Design, optimization and practical applications, in *SQUID sensors: fundamentals, fabrication and applications*, 179–233, Springer, 1996.
- [Car90] J. Carbotte, Properties of boson-exchange superconductors, *Reviews of Modern Physics*, **62**(4), 1027, 1990.
- [Che04] B. Chesca, R. Kleiner, D. Koelle, J. Clarke, and A. Braginski, Fundamentals and technology of squids and squid systems, *The SQUID Handbook, edited by J. Clarke and AI Braginski (Wiley-VCH, Weinheim, 2004)*, **1**, 128–148, 2004.

- [Cla04a] J. Clarke and A. I. Braginski, The SQUID handbook, Volume 1, 7, Wiley Online Library, 2004.
- [Cla04b] J. Clarke and A. I. Braginski, The SQUID handbook, Volume 1, Wiley Online Library, 2004.
- [Cla04c] J. Clarke and A. I. Braginski, The SQUID handbook, Volume 1, 46, Wiley Online Library, 2004.
- [Cla04d] J. Clarke and A. I. Braginski, The SQUID handbook, Volume 1, 63, Wiley Online Library, 2004.
- [Cla04e] J. Clarke and A. I. Braginski, The SQUID handbook, Volume 1, 65–70, Wiley Online Library, 2004.
- [Dru96a] D. Drung, F. Ludwig, W. Müller, U. Steinhoff, L. Trahms, H. Koch, Y. Shen, M. Jensen, P. Vase, T. Holst, et al., Integrated $yba2cu3o7-x$ magnetometer for biomagnetic measurements, *Applied Physics Letters*, **68**(10), 1421–1423, 1996.
- [Dru96b] D. Drung, Advanced squid read-out electronics, in *SQUID Sensors: Fundamentals, Fabrication and Applications*, 63–116, Springer, 1996.
- [Dru04] D. Drung and M. Mück, Squid electronics, *The SQUID Handbook: Fundamentals and Technology of SQUIDs and SQUID Systems*, **1**, 127–170, 2004.
- [Dru06] D. Drung, C. Hinnrichs, and H.-J. Barthelmess, Low-noise ultra-high-speed dc squid readout electronics, *Superconductor Science and Technology*, **19**(5), S235, 2006.
- [Dru10] D. Drung, J. Beyer, J.-H. Storm, M. Peters, and T. Schurig, Investigation of low-frequency excess flux noise in dc squids at mk temperatures, *IEEE transactions on applied superconductivity*, **21**(3), 340–344, 2010.
- [DW84] V. De Waal, P. Schrijner, and R. Llurba, Simulation and optimization of a dc squid with finite capacitance, *Journal of low temperature physics*, **54**, 215–232, 1984.
- [Enp86] K. Enpuku, K. Yoshida, and S. Kohjiro, Noise characteristics of a dc squid with a resistively shunted inductance. ii. optimum damping, *Journal of applied physics*, **60**(12), 4218–4223, 1986.
- [Ens05a] C. Enss, Cryogenic particle detection, Springer, 2005.

- [Ens05b] C. Enss and S. Hunklinger, Low-temperature physics, Springer Science & Business Media, 2005.
- [Fab18] B. Fabienne, Optimierung von gekoppelten dc-SQUIDs durch die Unterdrückung parasitärer Resonanzen und die Etablierung eines neuen Herstellungsprozesses für Nb/Al-AlOx/Nb-Josephson-Kontakte, 13–15, 2018.
- [Fer15] A. Ferring, Entwicklung von dc-SQUIDs zur Auslesung von metallischen magnetischen Kalorimetern, Masters Thesis, 2015.
- [Fey64] R. P. Feynman, R. B. Leighton, and M. Sands, The Feynman Lectures on Physics, Addison–Wesley, 1964.
- [Gin09] V. L. Ginzburg, V. L. Ginzburg, and L. Landau, On the theory of superconductivity, Springer, 2009.
- [Jos62a] B. D. Josephson, Possible new effects in superconductive tunnelling, *Physics Letters*, **1**(7), 251–253, 1962.
- [Jos62b] B. D. Josephson, Possible new effects in superconductive tunnelling, *Physics letters*, **1**(7), 251–253, 1962.
- [Jos64] B. Josephson, Coupled superconductors, *Reviews of Modern Physics*, **36**(1), 216, 1964.
- [Jos65] B. D. Josephson, Supercurrents through barriers, *Advances in Physics*, **14**(56), 419–451, 1965.
- [Kaa20] F. Kaap, Untersuchung des Einflusses von Kernspins und in Niob gespeichertem Wasserstoff auf das niederfrequente magnetische Flussrauschen in supraleitenden Quanteninterferenzdetektoren, Masters Thesis, 2020.
- [Kah24] N. Kahne, To be published, Masters Thesis, 2024.
- [Kem13] S. Kempf, A. Ferring, A. Fleischmann, L. Gastaldo, and C. Enss, Characterization of the reliability and uniformity of an anodization-free fabrication process for high-quality nb/al–alox/nb josephson junctions, *Superconductor Science and Technology*, **26**(6), 065012, 2013.
- [Kem15] S. Kempf, A. Ferring, A. Fleischmann, and C. Enss, Direct-current superconducting quantum interference devices for the readout of metallic magnetic calorimeters, *Superconductor Science and Technology*, **28**(4), 045008, 2015.

- [Kem16] S. Kempf, A. Ferring, and C. Enss, Towards noise engineering: Recent insights in low-frequency excess flux noise of superconducting quantum devices, *Applied Physics Letters*, **109**(16), 2016.
- [Kla04] T. Klapwijk, Proximity effect from an andreev perspective, *Journal of superconductivity*, **17**, 593–611, 2004.
- [Koc07] R. H. Koch, D. P. DiVincenzo, and J. Clarke, Model for 1/f flux noise in squids and qubits, *Physical review letters*, **98**(26), 267003, 2007.
- [Kui08] K. H. Kuit, J. Kirtley, W. Van Der Veur, C. Molenaar, F. Roesthuis, A. Troeman, J. Clem, H. Hilgenkamp, H. Rogalla, and J. Flokstra, Vortex trapping and expulsion in thin-film yba 2 cu 3 o 7- δ strips, *Physical Review B*, **77**(13), 134504, 2008.
- [Kum16] P. Kumar, S. Sendelbach, M. Beck, J. Freeland, Z. Wang, H. Wang, C. Y. Clare, R. Wu, D. Pappas, and R. McDermott, Origin and reduction of 1/f magnetic flux noise in superconducting devices, *Physical Review Applied*, **6**(4), 041001, 2016.
- [Lon50] F. London, Superfluids, Structure of matter series, Wiley, New York, 1950.
- [Maz24] D. Mazibrada, To be published, Masters Thesis, 2024.
- [McC68] D. E. McCumber, Effect of ac Impedance on dc Voltage-Current Characteristics of Superconductor Weak-Link Junctions, *Journal of Applied Physics*, **39**(7), 3113–3118, 1968.
- [Nyg28a] H. Nyquist, Thermal Agitation of Electric Charge in Conductors, *Phys. Rev.*, **32**(1), 110–113, 1928.
- [Nyg28b] H. Nyquist, Thermal agitation of electric charge in conductors, *Physical review*, **32**(1), 110, 1928.
- [Rus12] R. Russo, E. Esposito, C. Granata, A. Vettoliere, M. Russo, C. Cannas, D. Peddis, and D. Fiorani, Magnetic nanoparticle characterization using nano-squid based on niobium dayem bridges, *Physics Procedia*, **36**, 293–299, 2012.
- [Ryh92] T. Ryhänen, H. Seppä, and R. Cantor, Effect of parasitic capacitance and inductance on the dynamics and noise of dc superconducting quantum interference devices, *Journal of applied physics*, **71**(12), 6150–6166, 1992.
- [Sch19] C. D. Schötz, PolarmaXs: hochauflösendes, polarisationssensitives Röntgenspektrometer basierend auf magnetischen Mikrokalorimetern, PhD Thesis, 2019.

- [Sha49] C. E. Shannon, Communication in the presence of noise, *Proceedings of the IRE*, **37**(1), 10–21, 1949.
- [Ste06] K. Sternickel and A. I. Braginski, Biomagnetism using squids: status and perspectives, *Superconductor science and technology*, **19**(3), S160, 2006.
- [Sto21] R. Stoltz, M. Schmelz, V. Zakosarenko, C. Foley, K. Tanabe, X. Xie, and R. Fagaly, Superconducting sensors and methods in geophysical applications, *Superconductor Science and Technology*, **34**(3), 033001, 2021.
- [Tes77] C. D. Tesche and J. Clarke, Dc squid: Noise and optimization, *Journal of Low Temperature Physics*, **29**, 301–331, 1977.
- [Tes82] C. Tesche, Parameter fluctuations and low frequency noise in josephson junction devices, *Applied Physics Letters*, **41**(1), 99–100, 1982.
- [Vos81] R. F. Voss, Noise characteristics of an ideal shunted josephson junction, *Journal of Low Temperature Physics*, **42**, 151–163, 1981.
- [Wan18] Z. Wang, H. Wang, C. Y. Clare, and R. Wu, Hydrogen as a source of flux noise in squids, *Physical Review B*, **98**(2), 020403, 2018.
- [Wei69] M. Weihnacht, Influence of film thickness on dc josephson current, *physica status solidi (b)*, **32**(2), K169–K172, 1969.
- [Wel10] F. Wellstood, C. Urbina, and J. Clarke, Role of geometry on the color of flux noise in dc squids, *IEEE Transactions on applied superconductivity*, **21**(3), 856–859, 2010.

Erklärung

Ich versichere, dass ich diese Arbeit selbstständig verfasst und keine anderen als die angegebenen Quellen und Hilfsmittel benutzt habe.

Heidelberg, den 05.12.2023,


Fabian Krämer